

Sound scattering from a particle-laden, turbulent jet

Alex E. Hay

Department of Physics and Ocean Sciences Center, Memorial University of Newfoundland, St. John's, Newfoundland A1B 3X7, Canada

(Received 10 August 1990; accepted for publication 24 April 1991)

Multifrequency acoustic scattering experiments were carried out in the laboratory using a free, turbulent water jet carrying solid particles in suspension. A crossed-beam geometry was used, in which the axis of the jet was perpendicular, or nearly so, to the direction of the incident sound. The suspended particles were either natural sand grains or lead-glass beads, 100–500 μm in diameter. The results, based on measurements made simultaneously at 1, 2.25, and 5 MHz, include backscatter and attenuation as a function of suspended sediment concentration, measurements of the total scattering and backscattering cross sections of natural sand grains and glass beads as a function of frequency and particle size, and two-point correlation measurements of the fluctuations in apparent suspended sediment concentration. The lead-glass bead cross sections exhibit both the resonance and diffraction extrema expected of solid spherical scatterers; the sand cross sections do not and, for acoustic wavelengths comparable to or less than the particle circumference, are larger than spherical scatterer theory would predict. The two-point correlation estimates of jet velocity and measurements of the time-averaged jet width as a function of particle size are related to the mean and turbulent structure of two-phase jets and illustrate the potential of acoustic methods for noninvasive investigations of two-phase turbulent flow.

PACS numbers: 43.30.Ft, 43.30.Gv, 43.20.Fn

INTRODUCTION

The purpose of this article is to present results from a series of experiments on sound scattering by a turbulent, particle-laden jet, including both the time-averaged and fluctuating components of apparent particle concentration. While the motivation for the study arose initially from the problem of suspended sediment transport measurement in environments where fast-response sensors are a requirement, such as the wave-dominated nearshore zone, the results would appear to have broader application to the problem of particle concentration measurement in turbulent and nonturbulent two-phase flows in general.

A number of acoustic backscatter systems have been developed for suspended sediment transport studies in the oceanic benthic boundary layer.^{1–5} The main advantage of these devices is that it is possible to obtain suspended sediment concentration profiles at high temporal and spatial resolution with minimum disturbance to the near-bottom flow because the remote nature of the measurement allows the sensor to be placed some distance from the bed, usually 1–2 m. The main difficulty lies in inverting the backscattered signal to actual sediment concentration, a problem complicated by possible variations in particle size and by contamination of the signal by nonparticulate scatterers, such as air bubbles and biota.

The usual approach to the problem^{1,6} has been to calibrate the instrument as a function of concentration by creating a suspension along the entire acoustic path over a distance typically used in the field (~ 1 m), using the bottom sediments from the field site. While this approach has certainly proved useful, it does require that the additional attenuation due to particles in suspension along the sound

path, and the near- and far-field directivity patterns of the transducer, be properly taken into account. Furthermore, until now, calibrations have been carried out at a single acoustic frequency, and it must be assumed when applying such calibrations to field measurements that the size distribution of the particles in suspension is at all times and all heights above bottom the same as the size distribution of the particles on the bed.

In this article, results are presented from a different approach to the calibration problem, one in which a turbulent jet is used to maintain a statistically steady suspension localized along the sound path. This configuration permitted scattering measurements to be performed simultaneously at different frequencies using several single-frequency acoustic sounders, without needing to correct for scattering along the intervening path between the transducer and scattering volume. Furthermore, it is possible using the jet to confine the scatterers to the transducer far field and to conveniently measure the attenuation of the incident sound passing through the jet and the fluctuations in signal amplitude in relation to the turbulent structure of the flow field.

A primary aim of this paper is to illustrate the interplay that exists between the scattered sound field and dynamical properties of the jet. A turbulent jet with circular cross section was used, partly for simplicity of experimental design, but also because the fluid dynamics of such jets in the homogeneous, single-phase case are quite well known.⁷ The properties of two-phase jets are less well understood, even at low particle concentrations (less than a few percent by volume), although significant advances have been made recently.⁸ Furthermore, although acoustic scattering experiments with turbulent jets have been carried out in the single-phase case,^{9–11} I am not aware of any other study of sound scatter-

ing in a two-phase jet. Noninvasive measurements of particle concentration in two-phase jets have been made based on optical scattering,¹² to which acoustic methods would appear to offer an interesting alternative.

I. APPARATUS AND METHODS

The calibration tank is shown in Fig. 1. The suspended sediment jet is driven by a pump, and the jet velocity is controlled by a throttling section in the discharge line. The jet is discharged from a circular nozzle 2.0 cm in internal diameter, and the discharge velocity was 93 cm/s for the experiments reported here. This flow speed was sufficiently high that particles were not observed to settle in the horizontal segments of the return circuit, except for the largest particles used (425–500 μm diameter). The discharge Reynolds number, neglecting the effect of suspended particles on viscosity, was about 1.8×10^4 , assuring fully turbulent flow conditions in the return circuit and jet. At the base of the tank, the jet enters a receiving cone of circular cross section with an inlet diameter of 56 cm. The cone wall is inclined at 67° above the horizontal. Because of entrainment of ambient fluid into the jet, the volume transport in the jet exceeds that in the discharge, which is necessarily the same as the transport rate out of the base of the capture cone. This additional transport drives an upward return flow at the edge of the capture cone, and the deflection ring at the entrance to the cone reduces the associated loss of particles from the circuit. Thus an equilibrium state is established in the capture cone, consisting of a suspended sediment cloud and sediments settling on and avalanching down the cone wall, such that sediment is supplied by the jet and removed by the pump at equal rates.

Suspended sediment samples were drawn by suction through the J tube shown in Fig. 1. (This tube was moved to one side for the acoustic measurements.) The J tube inside diameter is 0.95 cm, and flow speeds in the tube were 150 cm/s, which greatly exceeds the maximum settling velocity of the particles used in this study (~ 8 cm/s for a 500- μm -diam sand grain), and is about four times the jet centerline velocity at the sampling point (~ 40 cm/s). These conditions meet the requirement¹³ that the suction velocity be greater than 1 m/s to avoid particle settling problems in the suction line for this particle size range and the requirement^{13,14} that the suction velocity be comparable to or greater than the speed of the external stream. Furthermore, the intake is oriented in the optimum direction:¹³ that is, into the flow. Thus the measured concentrations should be representative. Samples were drawn into 1- ℓ graduated cylinders, and concentrations were determined gravimetrically after filtering and drying the sample. Four replicate samples were drawn for each concentration measurement. The standard deviation of the four replicates ranged between 0.4%–13% and was typically 5%–7%, giving a standard error of 3% in the mean concentration.

The acoustic backscatter measurements were made at 1.0, 2.25, and 5.0 MHz using Mesotech model 810 immersible acoustic sounders, mounted as shown in Fig. 1, with the center of the measurement region 28 cm downstream of the discharge point. The configuration of the acoustic sounders

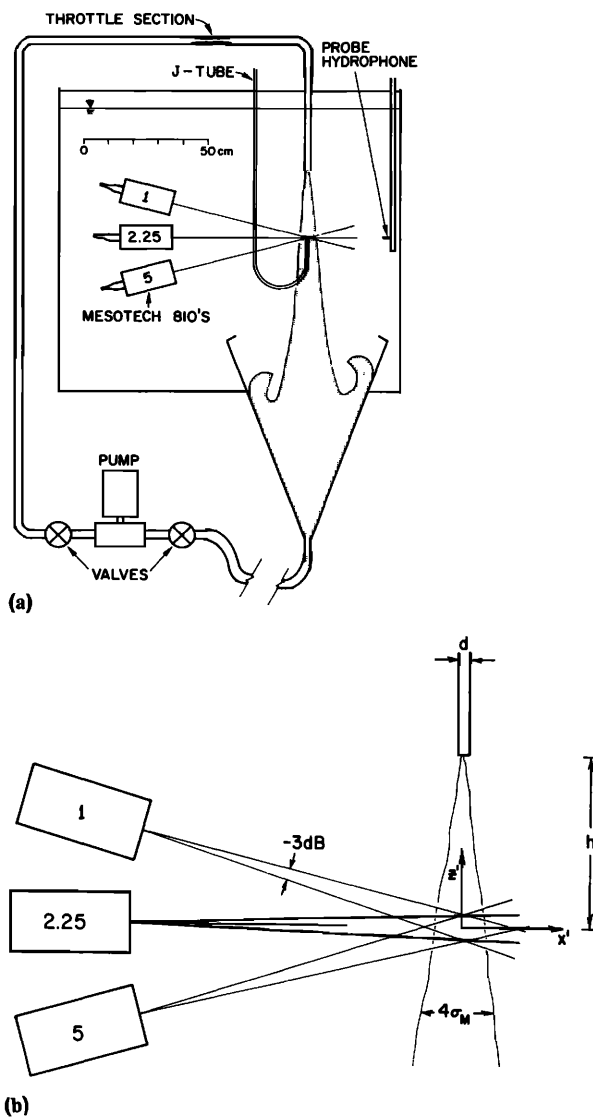


FIG. 1. (a) Sketch of experimental setup. Shading indicates suspended sediment jet and sediment cloud in capture cone. (b) Detail showing jet, -3-dB mainlobes of the transducer beam patterns, and coordinates relative to the scattering volume at the center of the jet.

as shown in Fig. 1 is not ideal (all three acoustic axes were better placed in the same horizontal plane), but was dictated by the size of the tank. The transmitted pulse is generated synchronously by applying a square wave burst across the single-element piezoceramic disk transducer with square-wave frequency equal to the transducer resonant frequency. The burst begins and ends on a zero crossing to reduce ringing. In these experiments, the burst duration was 20 μs , corresponding to a maximum possible range resolution of 1.5 cm. The received signal passes through a time-variable gain (TVG) amplifier, which corrects for spreading and attenuation, and is then heterodyned down to 455 kHz.

The pulse repetition rate and acquisition of the 455-kHz signals are controlled by a four-channel, computer-automated-measurement and control (CAMAC) crate-based data-acquisition system interfaced in these experiments to a Compaq 386/25 microcomputer. The 455-kHz signals were routed through an envelope detector (full-wave rectifier, low-pass filter) prior to analog-to-digital (A/D) conversion

at 200 kHz. The envelope detector was designed to have as low a threshold as possible, which, in practice, was 10–20 mV. The digitized backscatter signals from four consecutive pulses transmitted at 10-ms intervals were ensemble averaged and also block averaged over three adjacent sample points, giving a range resolution per stored sample of 1.1 cm and 12 digitized points averaged per stored sample. The averaging is done to reduce the amplitude of purely statistical fluctuations associated with the reconfiguration of particles from pulse to pulse. The four-ping ensemble-averaged backscatter profiles were acquired at rates of 6.5 Hz for three- or four-channel operation and 8.7 Hz for two-channel operation.

The 2-mm-diam piezoceramic probe hydrophone shown in Fig. 1 was used in conjunction with a LeCroy 9400 digital oscilloscope to map the directivity patterns of the Mesotech 810 and to measure the attenuation of the 2.25-MHz pulse by the jet during the backscatter experiments. Because the energy of the harmonics in the transmitted pulses was found to be large for the 1- and 2.25-MHz units particularly, the fast Fourier transform (FFT) capability of the oscilloscope was used to determine the directivity patterns of the fundamental and harmonics independently. The presence of the harmonics has not proved troublesome for the backscatter measurements, because of narrow-band filtering in the receiver electronics and has, indeed, provided a bonus by permitting attenuation to be measured at more than one frequency with a single unit. The attenuation measurements were made by first measuring the transmitted signal level with the jet off before each backscatter run and then during the run with the jet on. (No difference was found between transmitted signal levels with the jet off and with the jet on at zero particle concentration, and so scattering from the turbulence velocity fluctuations^{9–11} did not contribute measurably to the attenuation in these experiments.)

Velocity measurements were made with a Marsh-McBirney model 523 electromagnetic current meter, for which the sensing electrodes are mounted on a spherical probe 1.3 cm in diameter.

Both lead-glass beads and natural sands were used in the experiments. The properties of these lead-glass beads are well known¹⁵ with grain density, compression-wave speed, and shear-wave speed being 2870 kg/m³, 4870 m/s, and 2930 m/s, respectively. The sand was from three different locations (Queensland Beach, Nova Scotia; Bluewater Beach, Georgian Bay, Ontario; and Stanhope Lane Beach, Prince Edward Island) and was assumed to have the grain density of quartz: 2700 kg/m³. For size distribution determination for the natural sands and for separation into narrow size fractions, the particles were sieved through 20.3-cm-diam wire-mesh sieves following the methodology outlined by Carver,¹⁶ at $\frac{1}{4}\phi$ intervals (on the ϕ scale, the particle diameter in mm is given by $2^{-\phi}$). The size distribution parameters for these three sand types are presented in Table I.

II. THEORETICAL AND GEOMETRIC CONSIDERATIONS

In this section the theoretical formulation of the sound scattering problem for the transverse jet geometry is devel-

TABLE I. Size distribution parameters (in μm) for the natural sands used in the experiments, determined by sieving at $\frac{1}{4}\phi$ intervals: d_{50} represents the median diameter by weight; d_{16} and d_{84} the diameter of the 16th and 84th cumulative percentile, by weight, and represent \pm one standard deviation from the median of a log-normal distribution.

Source	d_{50}	d_{16} (μm)	d_{84}
Bluewater Beach	139	111	171
Stanhope Beach	157	129	189
Queensland Beach	360	275	460

oped. This geometry is determined by the directivity patterns of the acoustic transducers and by the suspended sediment concentration field in the jet, which is related to the dynamical behavior of free turbulent jets in general. In the following, most of the discussion concerns simple momentum jets, mention being made only where needed of the additional effects of buoyancy flux and of the sediments in suspension on the dynamics of the jet. It is assumed that the particle concentrations are low, of order 1% by volume or less, so that the suspension can be considered both dynamically and acoustically dilute. It is also assumed that the jet issues into a uniform, otherwise stagnant environment and that the only buoyancy flux is that due to the suspended sediment.

A. Suspended sediment jet characteristics

The mean velocity profile of a turbulent circular jet should be Gaussian at distances greater than six orifice diameters from the point of discharge (Ref. 17, p. 321). That is

$$W(x') = W_0 \exp(-x'^2/2\sigma^2), \quad (1)$$

where W is the time-averaged axial (in this case vertical) velocity, x' is the horizontal coordinate relative to the jet centerline [Fig. 1(b)], and W_0 is the mean centerline velocity. Measurements made with the electromagnetic current meter probe at the level of the 2.25-MHz transducer (14 orifice diameters downstream, Fig. 1), for centerline suspended sediment concentrations ranging from 0–5 kg/m³, are presented in Fig. 2 and show that Eq. (1) provides a reasonable fit to the data with $W_0 = 40$ cm/s and $\sigma = 2.2$ cm, apparently independent of concentration. This lack of mean velocity dependence on concentration is consistent with laser Doppler anemometry (LDA) measurements¹² in a particle-laden vertical water jet with comparable nozzle Reynolds number (~ 9000), using 500- μm -diam glass beads at concentrations up to 4.8% by volume at the discharge.

The centerline velocity varies with the distance h from the orifice as (Ref. 17, p. 324)

$$W(h) = 6.2W_0(0)d/h, \quad (2)$$

where d is the nozzle diameter, provided that $h \gg l_Q$, where l_Q is a characteristic length scale determined by the volume and specific momentum transports at the nozzle and is equal to $\sqrt{\pi/4}d$ for round jets. Here $l_Q = 1.8$ cm. From the previous section, $W_0(0) = 93$ cm/s, and Equation (2) gives $W_0 = 41$ cm/s, in agreement with the measured values in

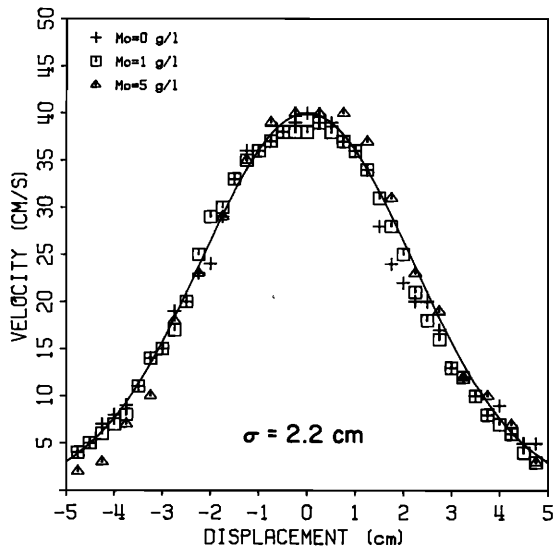


FIG. 2. Transverse profile of streamwise velocity component at 28 cm distance from nozzle. Symbols represent measurements at centerline concentrations of Bluewater Beach sand of 0 (+), 1 (\square), and 5 (\triangle) kg/m³. The solid line is a Gaussian profile, with $\sigma' = 2.2$ cm and $W'_0 = 40$ cm/s.

Fig. 2. Agreement was also obtained at a second distance ($h = 42$ cm), for which Eq. (2) gives 28 cm/s and the measurement gave 29 cm/s.

The rate of change of the characteristic jet width with h is

$$\sqrt{2}\sigma = 2\alpha_E h, \quad (3)$$

where α_E is an entrainment coefficient equal to 0.054 for jets.¹⁸ This relation gives $\sigma = 2.14$ cm at $h = 28$ cm, in agreement with the value of 2.2 cm from Fig. 2, especially since the larger measured value can reasonably be attributed to the finite spatial resolution of the current meter probe. The appropriate spatial weighting function for this device is not known. However, supposing for convenience that it is also Gaussian [i.e., $(\sqrt{2\pi}\hat{\sigma})^{-1}\exp(-x^2/2\hat{\sigma}^2)$], then the actual measured velocity profile can be shown to be

$$W'(x') = (\sigma/\sigma')W_0 \exp(-x'^2/2\sigma'^2), \quad (4)$$

where σ' is

$$\sigma' = (\sigma^2 + \hat{\sigma}^2)^{1/2}. \quad (5)$$

Setting $\hat{\sigma}$ equal to the probe radius (0.64 cm) as a first approximation and $\sigma' = 2.2$ cm (the measured value), Eq. (5) gives $\sigma = 2.11$ cm, in better agreement with the value predicted by Eq. (3). [Note also that the actual centerline velocity should be higher than the measured value by a factor σ'/σ : that is, $W_0 = 42$ cm/s instead of $W'_0 = 40$ cm/s at $h = 28$ cm. Both values are in equally good agreement with the 41-cm/s value given by Eq. (2).]

A suspended sediment concentration profile at $h = 28$ cm is shown in Fig. 3. Again, a Gaussian profile fits the data well, but the value of $\sigma'_M = 1.9$ cm (where the subscript M denotes the mass concentration) is less than the value of $\sigma = 2.1$ cm obtained from the velocity measurements. Furthermore, if one again attempts to account for the finite spatial resolution of the measurement by setting $\hat{\sigma} = 0.48$ cm,

the inside radius of the J tube, Eq. (5) gives $\sigma_M = 1.84$ cm, which is smaller still. This behavior, which is independently substantiated by the acoustic measurements to be presented, is opposite to that expected were the suspended sediment a passive scalar, in which case the characteristic width should have been 19% greater than that for momentum.^{17,18} The same effect has, however, been observed in other studies of turbulent, low-concentration, particle-laden jets directed vertically downward: for 500- μ m-diam glass beads in water using scattered light to determine particle number fluxes,¹² for 80–200- μ m-diam sand in air using direct sampling to determine particle mass flux,¹⁹ and for 50- and 200- μ m-diam glass beads in air.²⁰ The magnitude of the effect is much greater in the case of air jets, because of the much greater density difference between the solid and fluid phases. The value of σ_M is therefore determined at least in part by the finite settling velocity of the particles, which serves to reduce the time available for the particles to diffuse outward from the center of the jet during their descent.

The measurements in Fig. 3 were made with Bluewater Beach sand, with a median diameter of 140 μ m and 95% of the particles by weight below 250 μ m nominal diameter. The median and maximum settling velocities of these particles were therefore about 1.5 and 3.5 cm/s, respectively, assuming spherical shapes (Ref. 21, p. 177). These velocities are clearly non-negligible at the edge of the jet (see Fig. 2), especially for the larger particles. There seems to be no general relation between σ_M and σ as a function of settling velocity even for dilute particle concentrations in a jet. Nevertheless, if we consider a jet with uniform velocity and concentration profiles (the so-called top-hat profiles) and the relative widths of these profiles in a frame of reference moving at the speed of the velocity profile \bar{W}_0 , then it seems reasonable to propose on purely kinematical grounds that the width of the concentration profile should be reduced relative to that of the velocity profile by a factor $\bar{W}_0/(\bar{W}_0 + w_s)$, where w_s is the particle settling velocity. With $\bar{W}_0 = W_0/2$ (the velocity

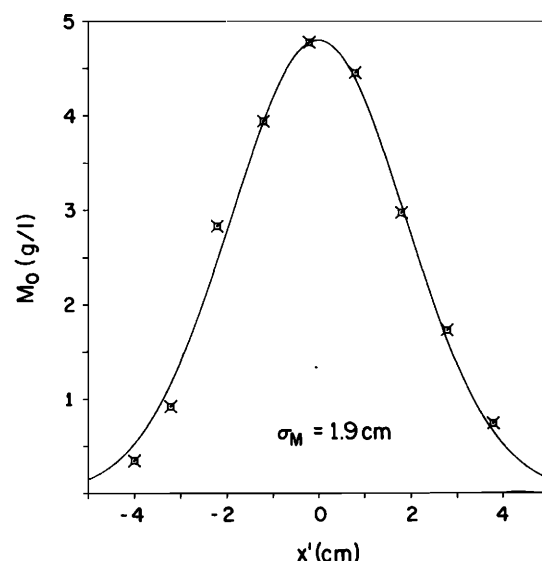


FIG. 3. Transverse particle concentration profile at 28 cm distance from nozzle, measured by suction using J tube. Solid line is a Gaussian profile with $\sigma'_M = 1.9$ cm and $M'_0 = 4.8$ kg/m³. Bluewater Beach sand.

averaged over a jet cross section of radius 2σ and $w_s = 3$ cm/s, this factor gives $\sigma_M = 0.87\sigma = 1.86$ cm. This value of σ_M is very close to the measured value, corrected for the spatial averaging of the measurement. It is concluded that $\sigma_M \approx 1.8$ – 1.9 cm for the measurements in Fig. 3 and that $\sigma_M/\sigma'_M \sim 0.95$, implying that the measured centerline suspended sediment concentrations may be about 5% low systematically, depending on particle size. Furthermore, the characteristic width of the concentration profile can vary with particle size.

B. Transducer beam patterns

For an ideal circular piston transducer of radius r_0 , the farfield directivity D is given by²²

$$D = 2J_1(k_c a_0 \sin \beta) / (k_c a_0 \sin \beta), \quad (6)$$

where J_1 is the cylindrical Bessel function of order 1, and $k_c = 2\pi/\lambda$ is the compression wave number in the medium,

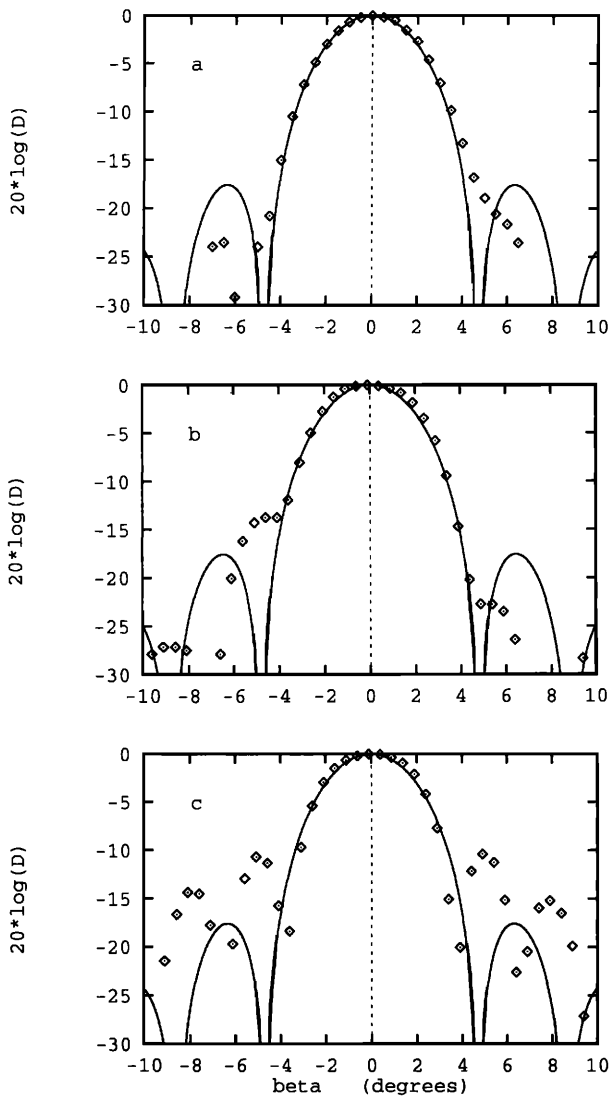


FIG. 4. Directivity patterns at (a) 1.00 MHz, (b) 2.25 MHz, and (c) 5.00 MHz. The symbols represent measurements made with the probe hydrophone and are the amplitude of the spectral peak at the fundamental frequency. The solid lines were computed from Eq. (6) using the values of a'_0 in Table II.

λ being the acoustic wavelength. Figure 4 shows the measured directivity patterns for the three different frequencies and those computed from Eq. (6) using not the actual radius of the piezoceramic disk, which is imbedded in epoxy, but an effective radius adjusted to give a good fit to the mainlobe of the beam pattern. In all three cases it was found that the effective radius so obtained was 15%–30% less than the actual transducer radius (Table II).

Examining Fig. 4, it can be seen that Eq. (6) does provide a reasonable fit to the mainlobe, which is of greatest importance here. The fit to the sidelobes is not good. Note also that the sidelobes for the 5-MHz unit are much higher than either the 1- or 2.25-MHz transducers. The -3 - and -12 -dB points on the mainlobes are listed in Table II, from which it can be seen that the beamwidths at all three frequencies are comparable, being about 4° between -3 -dB points, and about 7° between -12 -dB points.

Also listed in Table II are the distances from the transducer to the position of the last maximum in the amplitude of the transmitted pulse, measured along the acoustic axis. For a circular piston transducer, this should occur at a distance $r_1 = a_0^2/\lambda$ (Ref. 22, p. 153; Ref. 23), and furthermore measurements must be made at distances $r \geq \pi r_1$, if the far-field beam pattern given by Eq. (6) is to be used. It can be seen that the measured values of r_1 are comparable to a_0^2/λ .

C. Sound scattering from a suspended sediment jet

The geometry of the problem is sketched in Fig. 5, with the origin of the (x,y,z) coordinates at the center of the transducer, the surface of which is in the $y-z$ plane. The origin of the primed coordinates is in the center of the jet, with z' directed along the jet axis in the upstream direction. The x and x' axes are colinear.

The scattered pressure detected at a transducer a distance r from a single spherical particle of radius a is

$$\hat{p} = p_i \frac{f_\infty a}{2r} D \exp[i(k_c r - \omega t) - \alpha_0 r], \quad (7)$$

where f_∞ is the usual form factor,²⁴ ω is the angular frequency, α_0 is the linear attenuation coefficient in the medium, and p_i is the pressure amplitude of the incident wave. For an incident wave generated by a transducer with directivity D' at a distance r' from the particle, $p_i = p_* r_* D' \times \exp(-\alpha_0 r')/r'$, where p_* is the pressure at the reference distance r_* . For backscatter, $r = r'$ and $D = D'$. For a cloud of randomly moving particles with N particles per unit volume, waves scattered from individual particles will sum in-

TABLE II. Transducer beam pattern characteristics. Actual transducer radii are listed under a_0 , while a'_0 are the radii for which Eq. (6) provides the best fit to the measurements in the mainlobe. $\beta(-3)$ and $\beta(-12)$ are the mainlobe half-widths at -3 and -12 dB, respectively.

f (MHz)	a_0 (cm)	a'_0 (cm)	$\beta(-3)$ (deg)	$\beta(-12)$ (deg)	a_0^2/λ (cm)	r_1 (cm)
1	1.27	1.10	2.0	3.7	10.8	12.0
2.25	0.64	0.48	2.2	3.6	6.1	6.2
5	0.32	0.22	2.1	3.2	3.4	3.3

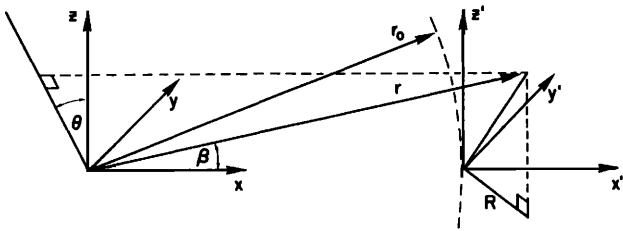


FIG. 5. Geometry of jet scattering problem.

coherently on average, and the mean-square scattered pressure will be $N\hat{p}^2$.

The mean-square pressure backscattered from an assemblage of uniformly sized spherical particles adopting random relative positions at constant concentration and detected using a pulsed system with pulse duration τ is therefore²⁵

$$\langle p^2 \rangle = p_*^2 r_*^2 \frac{|f_\infty|^2 a^2}{4} \int_{r_0 - c\tau/4}^{r_0 + c\tau/4} \int_0^{2\pi} \int_0^{\beta_m} ND^4 \frac{e^{-4\alpha r}}{r^2} \times \sin\beta \, d\beta \, d\theta \, dr, \quad (8)$$

where c is the speed of sound in the medium. The coordinates (r, θ, β) are defined in Fig. 5, and β_m is some maximum value of β chosen on the basis of the directivity pattern, such as the -3 -dB point, for example. The linear attenuation coefficient α is the sum of two parts:

$$\alpha = \alpha_0 + \frac{1}{r} \int_0^r \alpha_p \, dr, \quad (9)$$

with α_p being the additional attenuation due to the particles in suspension. For uniformly sized particles, α_p takes the form (Ref. 26, p. 441)

$$\alpha_p = N\Sigma_T/2, \quad (10)$$

where Σ_T is the total cross section of the particles, including, in general, both scattering and absorption effects.

For the special case in which N is independent of β and θ and constant in the range interval $r_0 \pm c\tau/4$, and for which $r_0 \gg c\tau/4$, Eq. (8) becomes

$$\langle p^2 \rangle = p_*^2 r_*^2 \frac{|f_\infty|^2 a^2}{4} \left(2\pi \int_0^{\beta_m} D^4 \sin\beta \, d\beta \right) \times r_0^{-2} \exp\left(-4\alpha_0 r_0 - 4 \int_0^{r_0} \alpha_p \, dr\right) \times \left(\frac{c\tau}{2} N(r_0) \frac{\sinh[(\alpha_0 + \alpha_{p0})c\tau]}{(\alpha_0 + \alpha_{p0})c\tau} \right), \quad (11)$$

where α_{p0} denotes the value of α_p at r_0 . The $\sinh[(\alpha_0 + \alpha_{p0})c\tau]/[(\alpha_0 + \alpha_{p0})c\tau]$ term accounts for the difference in amplitude of the scattered waves from particles, depending upon their position within the range interval $r_0 \pm c\tau/4$, because of absorption, and has often not been included in expressions relating backscatter intensity to suspended sediment concentration.

An interesting feature of Eq. (11), to which we shall have cause to return later, is that should particle concentrations ever become large enough that $\alpha_{p0}c\tau \gg 1 \gg \alpha_0c\tau$, then (11) can be shown to reduce identically to

$$\langle p^2 \rangle = p_*^2 r_*^2 \frac{|f_\infty|^2 a^2}{8\Sigma_T} \left(2\pi \int_0^{\beta_m} D^4 \sin\beta \, d\beta \right) \frac{e^{-4\alpha_0 r_0}}{r_0^2} \times \exp\left(-4 \int_0^{r_0 - c\tau/4} \alpha_p \, dr\right), \quad (12)$$

from which it is seen that the backscattered pressure from the range interval $r_0 \pm c\tau/4$ is then formally independent of the concentration of particles within this interval. Instead, it depends on the suspended particle concentration field only through the integrated particle attenuation along the intervening path: that is, for $0 < r < r_0 - c\tau/4$. Whether or not this rather curious result is actually realized in practice, as indeed appears to be the case in measurements to be presented, would seem to depend upon the importance of effects not considered in the derivation of Eq. (8), such as multiple scattering, at large $\alpha_{p0}c\tau$.

For the problem of scattering from the jet, N is not independent of θ and β , however, and, for the pulse duration used in these experiments ($20 \mu s$), is only approximately constant over a range interval $c\tau/2 = 1.5$ cm wide at the center of the jet, taking 1.8 cm for σ_N from the previous section. As a result, because $N(r, \theta, \beta)$ appears both as an integrated exponent and as a multiplicative factor in the integrand of Eq. (8), the integration is quite cumbersome and must be carried out numerically unless the jet concentration profile is wider than the mainlobe of the transducer beam pattern (see Appendix).

It is convenient to rewrite Eq. (8) in the form of Eq. (11): that is,

$$\langle p^2 \rangle = p_*^2 r_*^2 \frac{|f_\infty|^2 a^2}{4} \left(2\pi \int_0^{\beta_m} D^4 \sin\beta \, d\beta \right) \times \frac{e^{-4\alpha_0 r_0}}{r_0^2} \frac{c\tau}{2} N(r_0) e^{-A} \frac{\sinh B}{B} F, \quad (13)$$

where

$$A = 4 \int_0^{r_0} \alpha_p \, dr \cdots (\beta = 0) \quad (14)$$

and

$$B = (\alpha_0 + \alpha_{p0})c\tau \cdots (\beta = 0), \quad (15)$$

and F is a correction factor which depends on the departure of suspended particle concentration from uniformity with respect to (r, β, θ) in the range interval $r_0 \pm c\tau/4$. Note that when r coincides with the center of the jet, the case of interest here, A becomes

$$A = 2\sqrt{2}\pi\sigma_N(0)\alpha_{p0}, \quad (16)$$

where $\sigma_N(0)$ is the value of σ_N in the plane $z' = 0$.

In the general case, the correction factor F is given by

$$F = \frac{\int_{(r_0 - c\tau/4)}^{(r_0 + c\tau/4)} \int_0^{2\pi} \int_0^{\beta_m} ND^4 r^{-2} \exp(-4\alpha_0 r - 4 \int_0^r \alpha_p \, dr) \sin\beta \, d\beta \, d\theta \, dr}{2\pi \left(\int_0^{\beta_m} D^4 \sin\beta \, d\beta \right) r_0^{-2} \exp(-4\alpha_0 r_0) (c\tau/2) N(r_0) e^{-A} (\sinh B/B)}. \quad (17)$$

For the special case of uniform N in the interval $r_0 \pm c\tau/4$ and N independent of θ and β , then $F = 1$. For the special case of a

broad, cylindrical jet, which at low particle concentrations is a reasonable approximation to the conical jet geometry for sufficiently narrow beamwidths (see Appendix),

$$F \approx \left[\left(1 + \frac{A\gamma^2}{2} \frac{D_3}{D_1} + (A^2 + B^2) \frac{\gamma^4}{6} \frac{D_5}{D_1} + A(A^2 + B^2) \frac{\gamma^6}{24} \frac{D_7}{D_1} + [(A^2 + B^2) + 4A^2B^2] \frac{\gamma^8}{120} \frac{D_9}{D_1} + O(\gamma^{10}) \right) - B \coth B \left(\frac{\gamma^2}{2} \frac{D_3}{D_1} + 2A \frac{\gamma^4}{6} \frac{D_5}{D_1} + (B^2 + 3A^2) \frac{\gamma^6}{24} \frac{D_7}{D_1} + 4A(A^2 + B^2) \frac{\gamma^8}{120} \frac{D_9}{D_1} + O(\gamma^{10}) \right) \right], \quad (18)$$

where the D_n are the n th-order moments of D^4 , given by

$$D_n = \int_0^{\beta_m} D^4 \beta^n d\beta, \quad (19)$$

and γ is a parameter given by

$$\gamma = r_0 / \sqrt{2} \sigma_N(0). \quad (20)$$

The relative width of the jet and the acoustic beam is given by $\gamma\beta_m$, and (18) is derived assuming that

$$b_0 = \frac{\gamma\beta_m}{\sqrt{2}} = \frac{\beta_m r_0}{2\sigma_N(0)} < 1. \quad (21)$$

For the measurements to be presented, $r_0 \leq 55$ cm, so that $b_0 \leq 0.53$ using $\beta_m = \beta(-3 \text{ dB}) \sim 2^\circ$, and the inequality (21) is well satisfied between the -3 -dB points of the mainlobes.

The receiver output voltage is related to the received pressure at the transducer through an overall system sensitivity constant. From Eq. (13) the mean-square received voltage is

$$\langle v^2 \rangle = S_N^2 |f_\infty|^2 a^2 \frac{c\tau}{2} N(r_0) e^{-A} \frac{\sinh B}{B} F, \quad (22)$$

where S_N is the overall system constant, with dimensions of volts, given by

$$S_N = \chi P_* r_* \left(\frac{\pi}{2} \int_0^{\beta_m} D^4 \sin \beta d\beta \right)^{1/2}, \quad (23)$$

where χ is a constant, and it has been assumed that the time-variable gain (TVG) of the receiver has exactly compensated for the $r_0^{-2} \exp(-4\alpha_0 r)$ spreading and attenuation loss terms. In practice, this, of course, is not true, since the factory-set TVG parameters (c and α_0) will in general be different from the measurement conditions, and the acquired data must be recorrected appropriately. This was done using the relations given in Ref. 27 for α_0 and in Ref. 22 for c .

It is useful to rewrite Eq. (22) in terms of the mass concentration M of suspended sediment using $N = M / (4\pi a^3 \rho'_0 / 3)$, ρ'_0 being the grain density of the particles, so that

$$\langle v^2 \rangle = S_M^2 \frac{|f_\infty|^2}{a} \frac{c\tau}{2} \frac{M(r_0)}{\rho'_0} e^{-A} \frac{\sinh B}{B} F, \quad (24)$$

where $S_M^2 = 3S_N^2 / 4\pi$. For spherical particles with homogeneous elastic properties, f_∞ is a universal function of $X = k_c a$, so that it can be convenient to rewrite the first two factors in Eq. (24) as $S_M^2 k_c |f_\infty|^2 / X$. Finally, if a distribution of particle sizes is present, such that $N = \sum_j N_j(a_j)$, where the index j represents the j th size class, then assuming ρ'_0 is the same for all particles and the N_j are constant within $r_0 \pm c\tau/4$, Eq. (24) assumes the form

$$\langle v^2 \rangle = S_M^2 \frac{c\tau}{2} \frac{M(r_0)}{\rho'_0} \left(\sum_j \frac{|f_{\infty j}|^2}{a_j} m_j(r_0) \right) \times e^{-A} \frac{\sinh B}{B} F, \quad (25)$$

where the m_j are the mass-weighted size spectral densities defined by $M_j(r_0) = m_j M(r_0)$, and α_p is now given by $2\alpha_p = \sum_j N_j \sum_T$, instead of by Eq. (10). The important point here is that except for the $|f_\infty|^2/a$ term, Eqs. (24) and (25) are the same.

III. RESULTS

A. Backscatter amplitudes versus particle concentration

Typical results for the squared mean backscatter signal at the three frequencies as a function of suspended sand concentration are presented in Fig. 6 for Stanhope Beach sand. At each data point, the mean signal represents the average of 200 4-ping ensembles at the center of the jet, which was defined to be the range at which the mean backscatter amplitude reached a maximum value at low centerline concentrations, and the concentration is the average of 4 suction samples taken immediately after each backscatter run. The standard deviation of the 4-ping ensemble signal was typical-

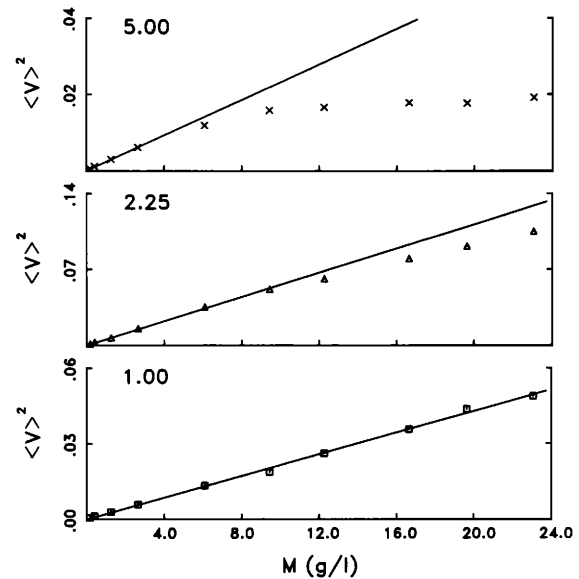


FIG. 6. Squared mean backscatter (in V^2) as a function of Stanhope Beach sand concentration at 1.00, 2.25, and 5.00 MHz. Straight lines were obtained by least-squares fit to all points at 1 MHz, the first six points at 2.25 MHz, and the first four at 5 MHz. $r_0 \sim 56$ cm.

ly 20%–30% of the mean, so that the average of 200 such ensembles gives a standard error of 1%–2% for the mean estimate, and 2%–4% for the squared mean. The standard deviation of the suction measurements ranged from 3.3%–8.9%, giving standard errors in the mean estimate between 1.6% and 4.5%. Error bars representing standard error are not shown in Fig. 6, because they are smaller than the symbols, except at large signal amplitudes and concentrations.

Figure 6 shows that at 1 MHz, the squared mean signal is linearly proportional to concentration, but that at both 2.25 and 5 MHz, departures from linearity occur at higher concentrations, and these departures are greatest at the highest frequency. This is in accordance with Eq. (24), which shows that in the absence of multiple scattering the mean-squared signal should be linearly proportional to particle concentration except when the attenuation due to particles is important. As will be seen, the departures from linearity in Fig. 6 are due to the increase of α_p with increasing frequency for these particles.

Figure 6 also shows that at 5 MHz the backscattered signal is virtually independent of the particle concentration at the center of the jet, at M_0 values greater than roughly 8 kg/m³, a possibility suggested earlier in relation to Eq. (12). Note that it is quite unlikely that this is an artifact caused by detector saturation. The detector saturation level, determined by clipping in the envelope detector, was 0.74 V, and as can be seen from the figure, the detected means are 0.14 V, well below this level. Note also in relation to the envelope detector that even though the threshold is low (10–20 mV), as mentioned in Sec. I, it is still important to take this threshold into account in the data processing to achieve the degree of linearity at low concentrations illustrated by Fig. 6.

Finally, although the squared mean signal is shown in Fig. 6, mean-square signal levels were also computed for these data. The differences were small, amounting only to the mean-square voltages being 5% higher than the squared means. Because squared mean computations are faster, an important data logging consideration particularly in field situations, results presented here are based on squared means.

B. Backscatter form factors for lead-glass beads and sand

Backscatter measurements were made as a function of particle size for both lead-glass beads and sand, a measurement of mean backscatter amplitude being made at only one particle concentration for each particle size. The objective of the lead-glass bead measurements was to determine the overall system sensitivity constant S_M in Eq. (24), making the assumption that the backscatter cross section for these particles could be accurately computed from the theory for scattering from a solid elastic sphere. Since good agreement with theory had been obtained previously for the total scattering cross section from attenuation measurements in suspensions of these same beads,¹⁵ this assumption seemed reasonable. The objective of the sand measurements was to measure the backscatter cross section for natural sand as a function of size and frequency, using the system sensitivity constants obtained from the lead-glass bead experiments.

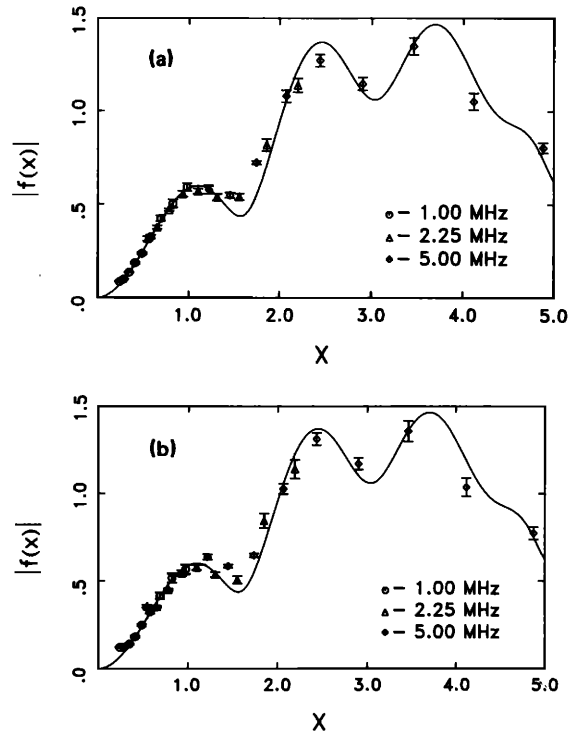


FIG. 7. Backscatter form factor $|f_\infty|$ for lead-glass beads, sieved into $\frac{1}{4}\phi$ size intervals, at 1.00 (○), 2.25 (△), and 5.00 (◇) MHz, (a) from “high”-concentration experiment and (b) from “low”-concentration experiment. Error bars are ± 1 standard error. Solid lines are theoretical form factor for lead-glass sphere in water. $X = k_c a$.

Two experiments were carried out using lead-glass beads, and the results are shown in Fig. 7 as $|f_\infty|$ plotted against $X = k_c a$, where a in this case is taken to be the midpoint of the $\frac{1}{4}\phi$ sieve interval. The measurements cover the size range 116–462 μm nominal diameter, nine sizes in all. Also shown in Fig. 7 is the theoretical form factor for a homogeneous lead-glass sphere in water, using the properties for this material given previously, and the nondissipative theory for scattering by a sphere.²⁸ These results, which show good agreement with theory including the diffraction extrema at $X = 1, 1.5, 2.4, 3.1,$ and 3.7 , and the first part of the minimum at the oblate-prolate resonance^{15,28} at $X \sim 5$ were obtained as follows. Examining Eq. (24), it is seen that, when α_p is negligibly small ($A, B \sim 0$),

$$\kappa \left(\frac{X \langle v^2 \rangle}{M_0} \right)^{1/2} = |f_\infty|, \quad (26)$$

where

$$\kappa = \frac{1}{S_M} \left(\frac{2\rho'_0}{k_c c \tau F} \right)^{-1/2}. \quad (27)$$

Since $\langle v^2 \rangle$ and M_0 are measured quantities and a is known, the value of κ for each frequency may be determined by a least-squares fit of the left-hand side of Eq. (26) evaluated from the measurements for each particle size, to the values of $|f_\infty|$ computed from theory for these sizes. This was done to produce Fig. 7, and the values of κ so obtained are listed in Table III. The two sets of measurements in Fig. 7 differ in the following respects. For those in Fig. 7(a), the same mass of

TABLE III. Sensitivity constants for the Mesotech 810 sounders from the lead-glass bead experiments, both high (H) and low (L) concentration. Measured water temperature and computed sound speeds were 21.5° and 1486.2 m/s for H and 22.3° and 1488.5 m/s for L .

Mesotech 810				
Unit	Frequency (MHz)		κ (kg/m^3) ^{1/2} /V	$S_M/(\rho'_0)^{1/2}$ V/(kg/m^3) ^{1/2}
A	1.00	H	5.36	2.35×10^{-2}
		L	5.31	
C	2.25	H	7.02	1.20×10^{-2}
		L	6.70	
B	5.00	H	13.0	0.434×10^{-2}
		L	12.5	

each size fraction was inserted into the circuit. This resulted in increasing centerline concentrations with increasing size (from 1.65 kg/m^3 for the smallest diameter particles to 6.4 kg/m^3 for the largest) because the relative amount of material contained in the suspension cloud in the capture cone decreases with increasing size and because the width of the jet (σ_M) decreases with increasing size. As a result, the measured on-axis attenuation was not always negligible, particularly for the larger sizes, the transmitted pulse amplitude decreasing by up to 20%–35% of its zero concentration value and a second series of measurements at lower centerline concentrations was run [Fig. 7(b)]. For this second experiment, concentrations ranged from 0.33 kg/m^3 for the smallest size to 1.02 kg/m^3 for the largest, and the measured on axis attenuation at 2.25 and 4.5 MHz did not exceed 5%. Comparing Fig. 7(a) and (b), the only significant difference is that in the low concentration experiment the points for the two smallest particle sizes lie above the theoretical curve. This is due to the lower accuracy of these data points, because of the smaller signal amplitudes for these particles at the reduced concentrations. It is encouraging that the values of κ are essentially the same for the two experiments, the differences being only 1%–5% (Table III).

A similar experiment was carried out using natural sand from the three sources listed in Table I, also sieved into $\frac{1}{4}\phi$ size intervals. As with the low-concentration glass bead experiment, the centerline concentrations were kept small, and the on-axis attenuation at 2.25 and 4.5 MHz did not exceed 7.5%. Centerline concentrations ranged from 0.65 kg/m^3 at the smallest size (98 μm diameter) to 1.11 kg/m^3 for the largest (463 μm diameter). The results for $|f_\infty|$, obtained from Eq. (26) using the glass bead values of κ corrected for the grain density of quartz [see Eq. (27)], are plotted in Fig. 8. It is gratifying that the estimates of $|f_\infty|$ are substantially the same for the three frequencies in the regions of overlap ($0.4 < X < 1$ for 1 and 2.25 MHz; $1.1 < X < 2.2$ for 2.25 and 5 MHz). Agreement with the theoretical curve, which was computed for a rigid movable sphere with the density of quartz [see Ref. 28(c)], is also quite good, especially for $X < 1$, and exhibits similar curvature in the interval $1 < X < 2$, though less pronounced. At higher values of X , the measured form factors are larger than predicted by the rigid movable spherical scatterer theory, and unlike the glass bead

case, there is no evidence of the higher-order diffraction extrema or of any resonance.

The choice of a rigid movable scatterer for the comparison in Fig. 8 is based upon the finding²⁹ that this provided the best fit of any spherical scatterer model to the then available measurements of the total scattering cross section for natural sand. Even so, as with the form factor measurements in Fig. 8, the measured total cross sections were greater than those given by theory, and no resonance features were present. We attributed these effects to grain shape irregularities, which are probably also responsible for the absence of diffraction oscillations in Fig. 8. (Note²⁵ that shape irregularities should not affect the scattering cross section in the long-wavelength region, $X \ll 1$). Also shown in Fig. 8 as a dashed line is the theoretical curve for a rigid, immovable (infinitely dense) sphere. Comparing this curve to the measurements in the vicinity of $X = 1$ indicates that the grain density (the only difference between the dashed and solid curves) can be important.

C. Backscatter measures of characteristic jet width (σ_M)

The width of the suspended sediment concentration profile, relative to the width of the mainlobe of the transducer directivity pattern, determines the degree to which the time-averaged particle concentration may be considered uniform throughout the detected volume, as embodied in the inequality (21). As pointed out earlier, the width of the concentration profile must depend on particle settling velocity and therefore on size, and possibly also on centerline concentration. To investigate these dependences, mean-square backscatter profiles were computed for the data from the sand and glass bead experiments in Figs. 6–8, and a Gaussian curve was fitted by least squares to five or seven adjacent 1.11-cm-wide range bins spanning the center of the jet. The results are presented in Fig. 9. Also shown in Fig. 9 are the curves $2.62 \bar{W}_0 / (\bar{W}_0 + w_s)$, where $\bar{W}_0 = 20$ cm/s as before, and w_s is the settling velocity for a lead-glass sphere or a quartz sphere for sand, as appropriate. The factor 2.62 comes from $1.19\sigma'$ with $\sigma' = 2.2$ cm, which is the width to be expected for a passive scalar contaminant ($w_s = 0$) on the

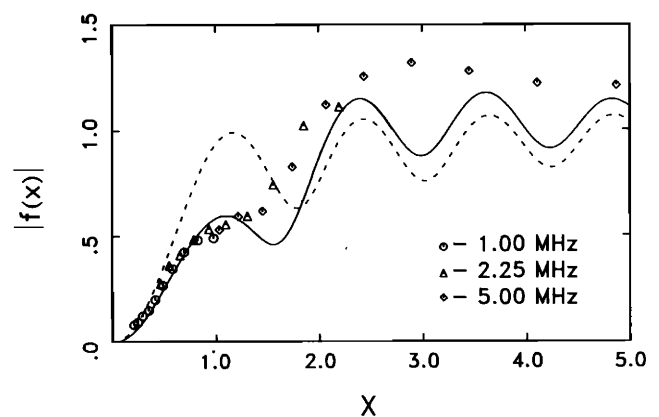


FIG. 8. Backscatter form factor $|f_\infty(\pi)|$ for natural sand, sieved into $\frac{1}{4}\phi$ intervals, at 1.00 (\circ), 2.25 (\triangle), and 5.00 (\diamond) MHz. The solid line is the theoretical form factor for a rigid sphere with the density of quartz; the dashed line that for a rigid sphere of infinite density. $X = k_c a$.

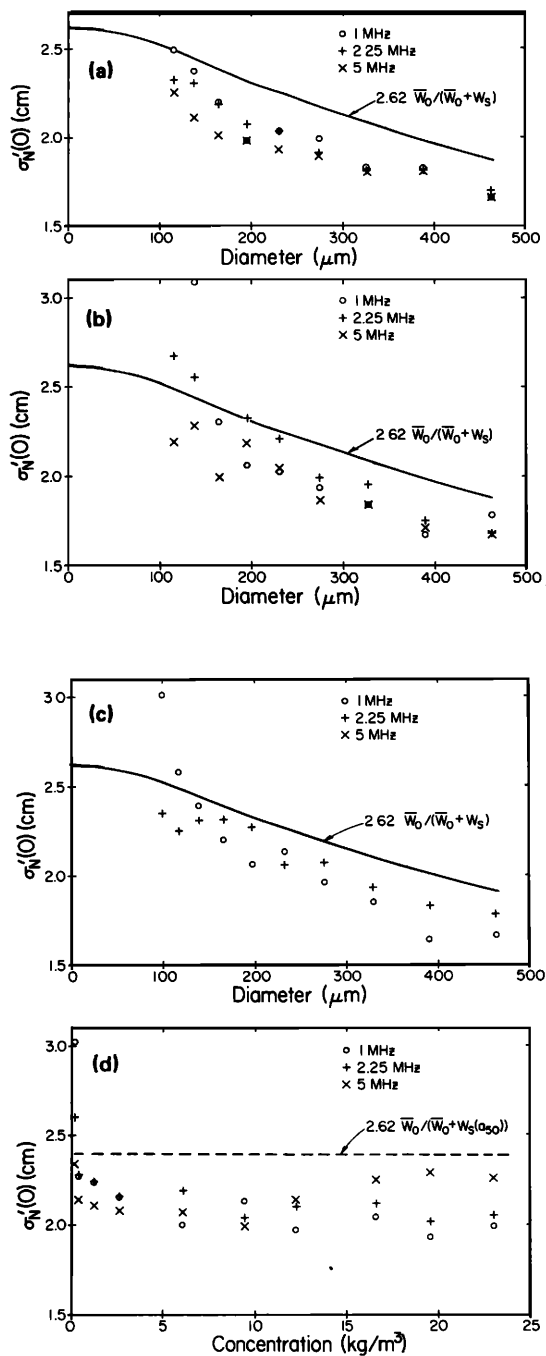


FIG. 9. $\sigma'_N(0)$ determined by least-squares fit of a Gaussian concentration profile to the mean-square backscatter amplitude profile of the jet, at 1.00 (O), 2.25 (+), and 5.00 (X) MHz for (a) lead-glass beads, "high" concentration; (b) lead-glass beads, "low" concentration; and (c) sand, as a function of size; (d) Stanhope Beach sand, as a function of centerline concentration.

basis of the measured velocity profile (Fig. 2), uncorrected for the spatial averaging effect of the measurement. Data points for all three frequencies are shown. The values of $\sigma'_N(0)$ for 1 and 5 MHz, which units were inclined at 15° to the horizontal (Fig. 1), are the values of σ'_N obtained from the fit, multiplied by the cosine of 15° .

The estimates of $\sigma'_N(0)$ as a function of particle size [Fig. 9(a)–(c)] at the three different frequencies are quite

consistent with each other for particles larger than about $140 \mu\text{m}$ diameter for all three experiments. Furthermore, and again considering sizes $> 140 \mu\text{m}$, the manner in which σ'_N decreases with increasing size is quite similar for the three experiments and remarkably consistent with the simple relation $\sigma'_N = 2.62 \bar{W}_0 / (\bar{W}_0 + w_s)$. For particles less than $140 \mu\text{m}$, the estimates are high and more erratic, particularly at 1 and 2.25 MHz. This is again attributed to the small signal levels at these frequencies for the concentrations used in these experiments. Figure 9(d) shows $\sigma'_N(0)$ as a function of particle concentration for the Stanhope sand experiment in Fig. 6. Again, at low concentrations the estimates tend to be larger, particularly at 1 and 2.25 MHz, than for concentrations above 2 kg/m^3 . For $2 < M < 13 \text{ kg/m}^3$, the values for all three frequencies are similar, whereas for $M > 15 \text{ kg/m}^3$, the 5-MHz estimate tends to be larger than the other two. This is due to attenuation, which is greatest at 5 MHz for Stanhope sand and broadens the mean-squared backscatter profile. Neglecting therefore the 5-MHz values at high concentrations, it is concluded that $\sigma'_N(0)$ may decrease slightly, but is essentially constant over this concentration range.

D. Attenuation versus particle concentration

It has already been mentioned with respect to the experimental configuration in Fig. 1 that attenuation was measured at the fundamental and first harmonic of the 2.25-MHz unit. The voltage output from the hydrophone at a distance r_H from the transmitter is, for a given frequency and centerline particle concentration, given by $v_H(\omega, M_0) = \text{const} \times r_H^{-1} \exp(-\alpha_0 r_H - A/2)$, where $\exp(-A/2)$ is the attenuation due to particles across the full width of the jet, and A is given by Eq. (16). One obtains therefore

$$A(\omega)/2 = \sqrt{2\pi} \sigma'_N(0) \alpha_{p0}(\omega, M_0) = \ln[v_H(\omega, 0)/v_H(\omega, M_0)], \quad (28)$$

where, as mentioned in Sec. II, $v_H(\omega, 0)$ was measured with the jet off before each backscatter run.

The results of such measurements for Stanhope sand, each point taken from the average of the spectra from 50 pings, are presented in Fig. 10. These data are from the same experiment as the backscatter data in Fig. 6, and the $\sigma'_N(0)$ results in Fig. 9(d). It can be seen that at 4.5 MHz the measurements are quite linear for all concentrations and at higher concentrations for 2.25 MHz. At 2.25 MHz the attenuation at low concentrations is weak and the change in signal amplitude was undetectable in our setup. This is also the reason that the measured attenuation at this frequency is negative at low concentrations, an otherwise improbable result.

The linearity of the attenuation measurements in Fig. 10, together with the near constancy of $\sigma'_N(0)$ in Fig. 9(d), indicates that α_{p0} increases linearly with concentration and therefore that multiple scattering is not important over this particle concentration range. This is not an unexpected result, since particle concentrations are low, less than 1% by volume. (See, for example Ref. 30 for a discussion of the subject and for theoretical computations of multiple-scattering effects on attenuation as a function of concentration for quartz spheres in water.)

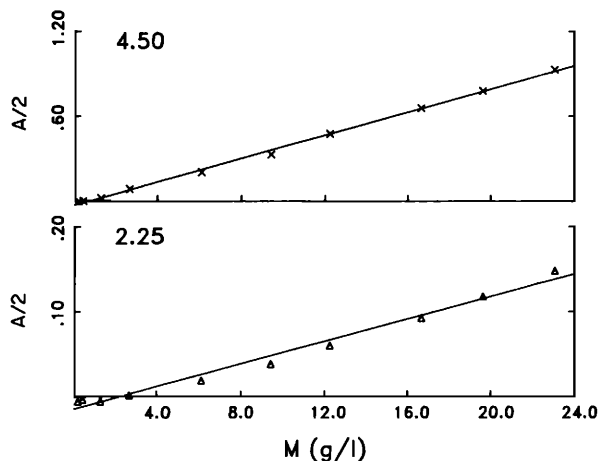


FIG. 10. Measured axial attenuation through the jet, at the fundamental and first harmonic of the 2.25-MHz unit, as a function of centerline concentration for Stanhope Beach sand. Solid lines represent linear least-squares fit.

E. Total scattering cross sections

Using Eqs. (29) and (10), the total cross section can be computed from the attenuation measurements when $\sigma'_N(0)$ is known. It is convenient to express this in the form²⁸

$$\frac{\alpha\alpha_{p0}}{\epsilon_0} = \frac{\rho'_0 aA/2}{\sqrt{2\pi}\sigma'_N(0)M_0}, \quad (29)$$

where $\epsilon_0 = M_0/\rho'_0$ is the volume concentration at the jet centerline, and $\alpha\alpha_{p0}/\epsilon_0 = 0.75\Sigma_T/(2\pi a^2)$ for uniformly sized particles, which tends to 0.75 as X tends to infinity.

Figure 11(a) shows the results from the high-concentration lead-glass bead experiment, using the 2.25-MHz values of $\sigma'_N(0)$ from Fig. 9(a). The measurements follow the general form of the theoretical curve for a lead-glass sphere rather well, but with significant departures on a point-to-point basis. These are unlikely to represent real departures from spherical scatterer theory since excellent agreement with theory has been found in more accurate measurements¹⁵ for the same particle type. Figure 11(b) shows the values of $\alpha\alpha_{p0}/\epsilon_0$ as a function of size for natural sand, computed using the values of $\sigma'_N(0)$ at 2.25 MHz in Fig. 9(c). Except at small values of X , the general trend of the data is for the total cross section to be larger than the total scattering cross section for a rigid movable sphere with density $\rho'_0 = 2700 \text{ kg/m}^3$ (the solid line in the figure). This is in agreement with our previous finding,²⁹ where it was also shown that a better fit to the then available data for the total cross section of natural sand is provided by a modified form of the so-called high-pass model.³¹ The modified high-pass model is given by²⁹

$$\alpha\alpha/\epsilon = \kappa_\alpha X^4/[1 + (4\kappa_\alpha/3)X^4 + X^2], \quad (30)$$

with $\kappa_\alpha \approx 0.2$ for quartz in water, and the measurements in Fig. 11(b) confirm that it does provide a better fit. However, as with the glass bead data, there is substantial scatter among the data points about the expected best-fit curve.

The most likely reason for the scatter in the cross section data in Fig. 11 is statistical. The number of spectra (50, the

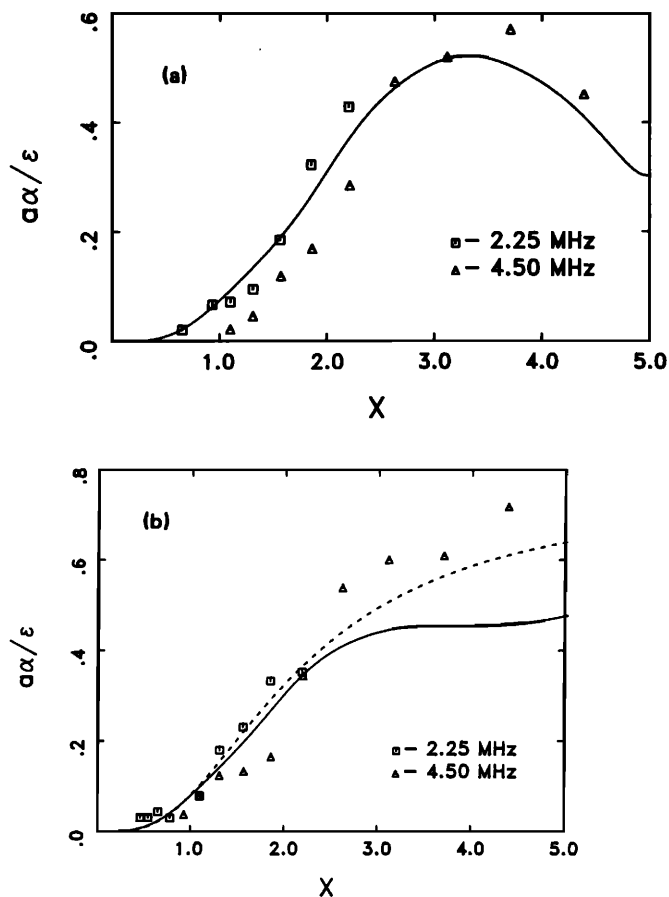


FIG. 11. Normalized total cross sections, plotted as $\alpha\alpha/\epsilon = 0.75\Sigma_T/2\pi a^2$, for (a) lead-glass beads ("high"-concentration experiment) and (b) sand, at 2.25 (\square) and 4.50 (\triangle) MHz. Solid line in (a) is theory for lead-glass sphere. Solid line in (b) is theory for rigid sphere with density of quartz; dashed line is the modified high-pass model.

number that could be acquired during a 200 4-ping ensemble backscatter run) used to obtain the mean attenuation estimate was insufficient. This is confirmed by Fig. 12, which is a plot of the total cross section for unsieved Bluewater, Stanhope, and Queensland sand, computed from the slope of attenuation measurements as a function of concentration like those in Fig. 10, using an average value of $\sigma'_N(0)$ computed from data such as those in Fig. 9(d). These data points therefore represent an average of 500–600 pings (10–12 concentrations were used in each experiment) and cluster much more tightly about the high-pass model curve. Statistical inaccuracies in the estimate of $\sigma'_N(0)$ could also contribute to the scatter, but it is worth noting that systematic errors of the type discussed previously with respect to the finite spatial resolution of the measurements should not. This is because the diameter of the J tube (0.95 cm) is approximately the same as the width of the range bins (1.11 cm) and $c\tau/2$ (1.5 cm), so that the product $M_0\sigma'_N(0)$, which appears in Eq. (29), should be nearly the same as $M'_0\sigma'_N(0)$ [see Eq. (4)].

F. Attenuation correction

The measured values of A can be used to compute the correction factor $Be^A/\sinh B$, which, by Eq. (24), would

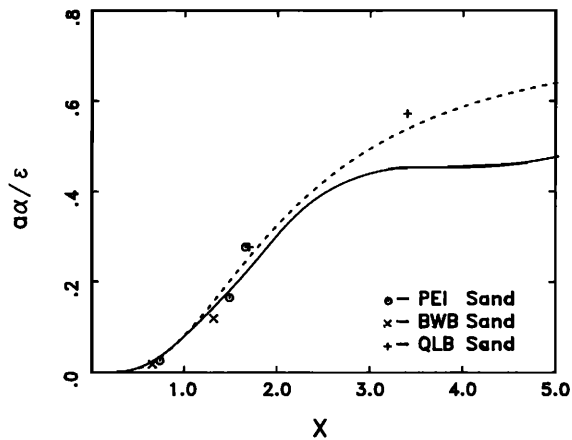


FIG. 12. Normalized total cross sections for Stanhope Beach sand at 2.25, 4.5, and 5 MHz (O) and for Bluewater Beach sand (X) and Queensland Beach sand (+) at 2.25 and 4.5 MHz.

remove the effects of α_p from the mean-square backscatter signals except for the α_p dependence of F . This assumes, of course, that the mainlobe of the directivity pattern is much narrower than the particle concentration profile in the jet. Figure 13 shows the result of applying this correction to the 2.25- and 5-MHz backscatter signals in Fig. 6, using the 2.25- and 4.5-MHz attenuation measurements in Fig. 10. It can be seen that while the 2.25-MHz signal is now linear, the 5-MHz signal is overcorrected, even though the total scattering cross section at 4.5 MHz is less than that at 5 MHz for Stanhope Beach sand (Fig. 12).

The on-axis attenuation is obviously greater than the average attenuation in the mainlobe of the directivity pattern, an effect incorporated in the geometric correction factor F which has not yet been considered explicitly, so that some overcorrection is to be expected. Nevertheless, it was clear from this result that direct measurements of the attenuation at 5 MHz were necessary. Therefore, the positions of the 2.25- and 5-MHz units in the tank were interchanged, and two more experiments were carried out using Stanhope Beach sand, one at long range ($r_0 = 53$ cm) and one at short range ($r_0 = 25.7$ cm). The results of these experiments are

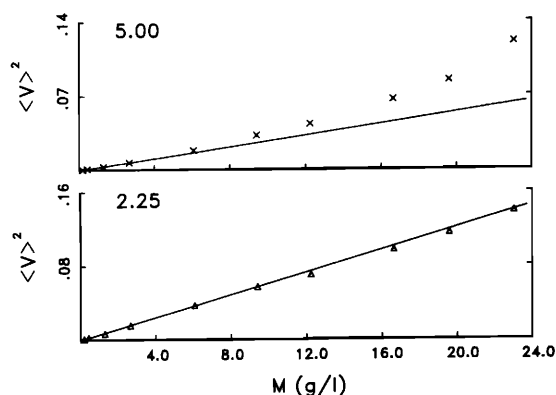


FIG. 13. Stanhope Beach sand, 2.25- and 5.00-MHz squared mean backscatter intensities (in V^2) from Fig. 6, corrected for attenuation, with $F = 1$.

presented in Fig. 14. These attenuation measurements [Fig. 14(a) and (b)], in this case obtained from the average of 100 spectra (pings), are again highly linear over this concentration range, at both short and long range, and also provide an example of the repeatability of the attenuation measurement: The slopes of the straight lines in Fig. 14(a) and (b), obtained by least-squares fit differ by less than 6%.

The backscatter measurements are shown in Fig. 14(c) and (d). Again, the squared mean backscatter amplitude tends to be independent of concentration for $M_0 \gtrsim 10$ kg/m³, as in Fig. 6, and this may now be examined quantitatively. From Eqs. (15) and (16), $B \approx A c \tau / 2 \sqrt{2 \pi} \sigma_N(0)$, since $\alpha_0 c \tau$ is negligible at these frequencies; so with $\sigma_N(0) \approx 2$ cm, $B \approx 0.6 A / 2$, and from Fig. 14, $B \approx 0.9$ maximum, for these measurements. Now, by letting $C = A - B$ be the exponent for the attenuation correction up to $r_0 - c \tau / 4$, we have

$$e^{-A} \frac{\sinh B}{B} = e^{-C} \left(\frac{1 - e^{-2B}}{2B} \right). \quad (31)$$

When $B \gg 1$, this becomes $e^{-C} / 2B$, in which case Eq. (24) becomes independent of M_0 , like Eq. (12). When $B = 0.9$, $(1 - e^{-2B}) / 2B \approx 1 / 2B$ (17% error), and so it is reasonable that $\langle v^2 \rangle$ should be approximately independent of M_0 at these concentrations, although the degree of independence exhibited in Figs. 6 and 14(c) is greater than expected on the basis of this argument. Perhaps the factor F or concentration fluctuations plays a role.

The data in Fig. 14(a) and (b) also provide additional information on the repeatability of the backscatter measurement. Table IV summarizes the results from four experi-

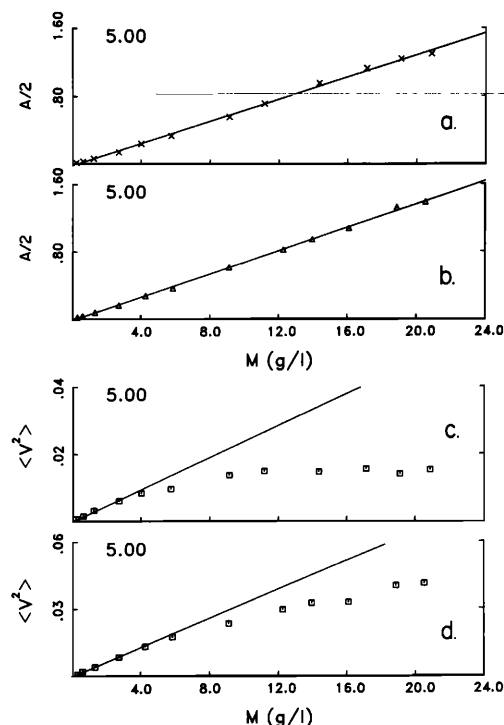


FIG. 14. Stanhope Beach sand, axial attenuation at 5 MHz across the jet for (a) $r_0 = 26.2$ cm and (b) $r_0 = 53.0$ cm, and squared mean backscatter amplitude (in V^2) at 5 MHz for (c) $r_0 = 26.2$ cm and (d) $r_0 = 53.0$ cm. In (a) and (b), solid lines are from least-squares fit to all points; in (c) and (d) from least-squares fit to the first four points.

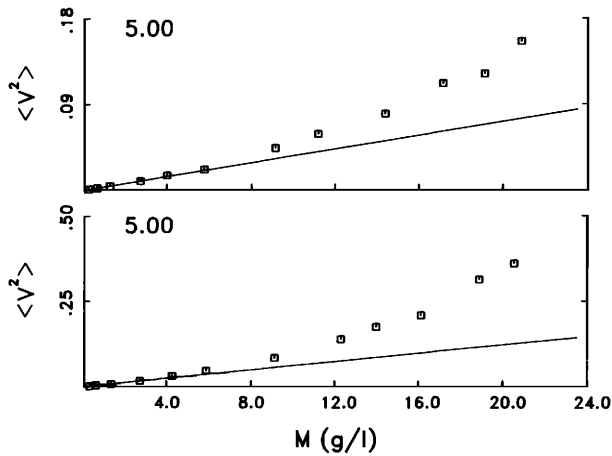


FIG. 15. Stanhope Beach sand, squared mean backscatter corrected for attenuation, with F taken from the Appendix. Top panel corresponds to Fig. 14(c), bottom panel to Fig. 14(d). Solid lines obtained by least-squares fit to the first four points.

ments with Stanhope Beach sand. Listed are the slopes obtained by linear least-squares fit to the indicated number of points in the low-concentration range of the measurements (all points were used for 1 MHz). The first two experiments are in good agreement, the maximum difference being less than 4%. This is consistent with the repeatability inferred earlier from the lead-glass bead backscatter measurements (Fig. 7 and Table III). For the third experiment listed in Table IV, however, the measurements at all three frequencies are systematically higher, by 14% at 1 and 2.25 MHz and by 30% at 5 MHz, than the average of the first two experiments. Also, the short-range experiment, for which no 1- or 2.25-MHz data were collected because of the larger inclination angles at short range and possible near-field complications (Table II), is in much better agreement with the first two experiments. Since the third experiment involved interchanging the 2.25- and 5-MHz units and the fourth involved moving the 5-MHz unit closer to the jet, these differences point to possible mechanical alignment problems in the apparatus.

Returning now to the 5-MHz attenuation correction, applying the correction $Be^A/\sinh B$ to the backscatter data in Fig. 14(c) and (d) [using the attenuation measurements in Fig. 14(a) and (b)], again resulted in an overcorrection similar to that in Fig. 13, only more severe, as the reader may

verify. This is not simply an effect of the geometry for, even when the geometric factor F is computed including the large 5-MHz sidelobes in the numerical integration and even though this correction is large (amounting to almost a 40% reduction of $Be^A/\sinh B$ at the highest concentrations measured; see the Appendix), it is not large enough. Figure 15 shows the backscatter results, corrected including the factor F , from which it can be seen that the backscatter is still overcorrected at both ranges, and this in spite of the fact that at the shorter range the axial attenuation measurement should be more directly applicable for all values of β within the mainlobe.

The explanation for the remainder of the overcorrection is believed to reside in the turbulent fluctuations in particle concentration across the jet. Stated simply, because the attenuation correction is nonlinear when the attenuation is large ($A \gtrsim 1$), correcting the averaged backscatter using the average attenuation will not give the correct result. Instead, the instantaneous backscatter must be corrected using the instantaneous attenuation, before averaging.

G. Fluctuations in backscatter amplitude: Two-point correlations

The fluctuations in the backscatter signals are large. Time series of backscatter from the edge of the jet at 2.25 and 5 MHz are presented in Fig. 16. These data were acquired at a 4-ping ensemble-averaged rate of 8.7 Hz (2-channel operation), with a total of 1200 ensembles acquired for the run, using Queensland Beach sand at a centerline concentration of 6.43 kg/m^3 . The 5-MHz unit was mounted below the 2.25-MHz unit with both beams directed horizontally in the same vertical plane, separated by a vertical distance of 13.5 cm (Fig. 16).

The amplitude fluctuations in Fig. 17 span one to two orders of magnitude. Similar "spikiness" has been observed in field measurements from the nearshore zone using both optical backscatter^{32,33} and acoustic backscatter.^{1,5,34} Because fluctuations of this magnitude must necessarily represent a dominant flux term in the sediment transport rate, it is essential to know the degree to which these variations in apparent concentration are real. Equally, the previous discussion of concentration fluctuations with respect to the attenuation correction implies that instantaneous (ensemble-averaged) backscatter profiles must be inverted to concentration before averaging over longer time periods,

TABLE IV. Results from repeated measurements of backscatter from Stanhope Beach sand. The experiment designation is the year (89) followed by the Julian day of the experiment. The numbers in parentheses for each slope represent the number of points used in the fit.

Experiment	1.00 A		2.25 C		5.00 B	
	r_0 (cm)	slope $V^2/m^3/kg$	r_0 (cm)	slope $V^2/m^3/kg$	r_0 (cm)	slope $V^2/m^3/kg$
89222	56.6	2.15×10^{-3} (10)	55.5	5.59×10^{-3} (6)	56.6	2.32×10^{-3} (4)
89228	57.2	2.23×10^{-3} (12)	54.9	5.43×10^{-3} (8)	56.1	2.37×10^{-3} (4)
89261	55.2	2.50×10^{-3} (12)	55.2	6.26×10^{-3} (8)	53.0	3.05×10^{-3} (4)
89263	26.2	2.25×10^{-3} (4)

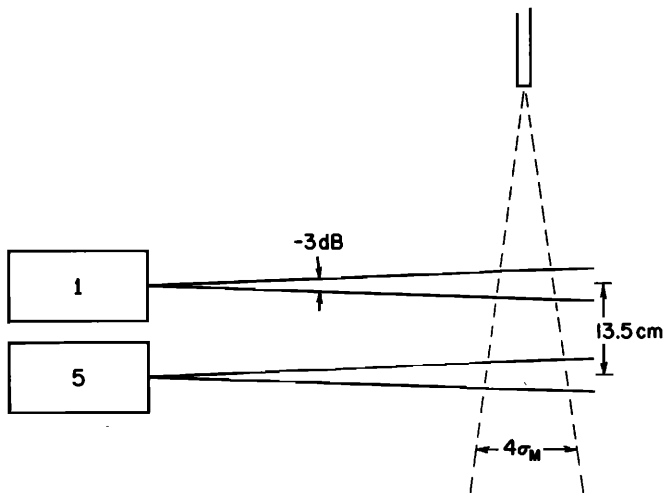


FIG. 16. Configuration for two-point correlation measurements.

which implies that rather narrow confidence limits are required for the relationship between instantaneous backscatter amplitudes and actual concentrations, especially when the attenuation is large.

The purpose of the present experiment was to investigate whether or not the backscatter amplitudes at two points separated in the streamwise direction are correlated at lags

related to the vertical separation and streamwise velocity. Such a correlation would be expected if the spikes in Fig. 17 are due to discrete eddies being advected through the sound beams. The normalized cross-correlation function between the two records in Fig. 17 is presented in Fig. 18, and, while not large, there is a peak centered at a lag of about 1 s, which corresponds to a velocity of 13.5 cm/s, a reasonable value at the edge of the jet (Fig. 2). The cross-correlation function was computed for range-bin pairs across the jet, starting with pairs at the edge of the jet nearest the transducers and working across. Because of entrainment, the jet was wider at the 5-MHz level than at the 2.25-MHz level (Fig. 16). This increase in width is reflected in the transverse profiles of backscatter amplitude in Fig. 19(a). As a result, for each 2.25-MHz bin not at the center of the jet ($r_0 = 54.6$ cm), a correlation function was computed for two or three of the underlying 5-MHz range bins. The peak in the two-point correlation function already less than 0.3 at the edge of the jet (Fig. 18), decreased in magnitude toward the center of the jet to become almost imperceptible there, presumably because the 8.7-Hz sampling rate and 4° beamwidths were barely able to resolve even the largest eddies at the center of the jet.

The resulting velocity profile is presented in Fig. 19(b) and should represent the mean velocity midway between the two sounders. It is therefore compared with the profile computed from that in Fig. 2 for $h = 35.25$ cm using Eqs. (1)–(3). Each two-point correlation velocity is plotted at a range

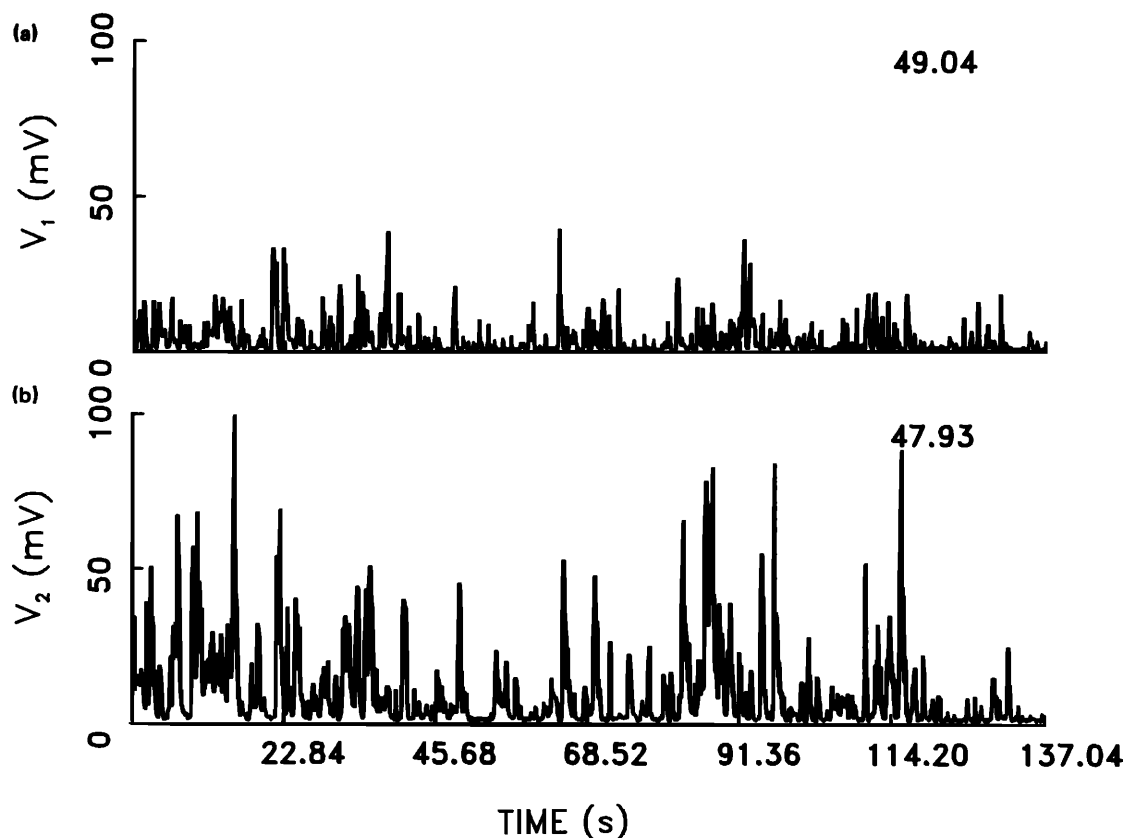


FIG. 17. Time series of backscatter amplitude from the edge of the jet at (a) 2.25 MHz, $r = 49.04$ cm and $h = 28$ cm, and (b) 5.00 MHz, $r = 47.93$ cm, and $h = 41.5$ cm. Queensland Beach sand.

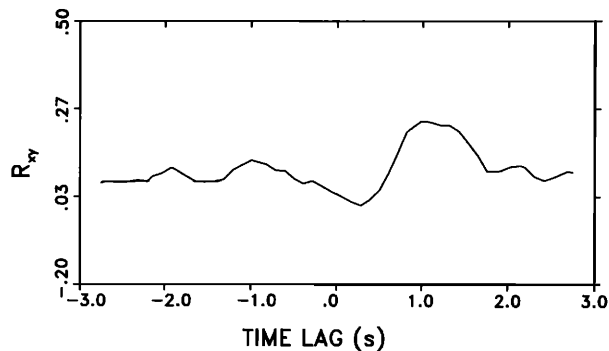


FIG. 18. Normalized cross correlation of Fig. 17(b) lagged with respect to Fig. 17(a). Positive lag means that 17(b) lags 17(a).

equal to the average of the ranges for each 2.25/5-MHz range-bin pair. The two-point correlation velocity estimates are reasonable in the sense that they are in the range expected from the measured mean velocity profile. In the vicinity of the centerline, for example, the correlation values are quite comparable to those extrapolated from the direct measurements at $h = 28$ cm, particularly on the near side of the jet. In the wings of the profile (i.e., 5 cm from the jet center and beyond), the correlation estimates are higher than the extrapolated mean velocities, but since eddies carrying larger than average concentrations from the core region of the jet

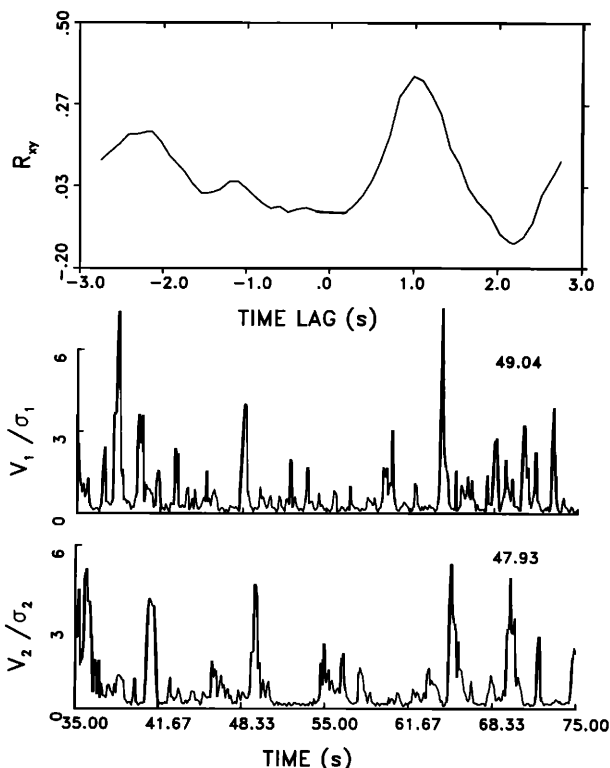


FIG. 20. Backscatter amplitude time series, normalized variance, and cross-correlation function for the 35–75-s segment of Fig. 18.

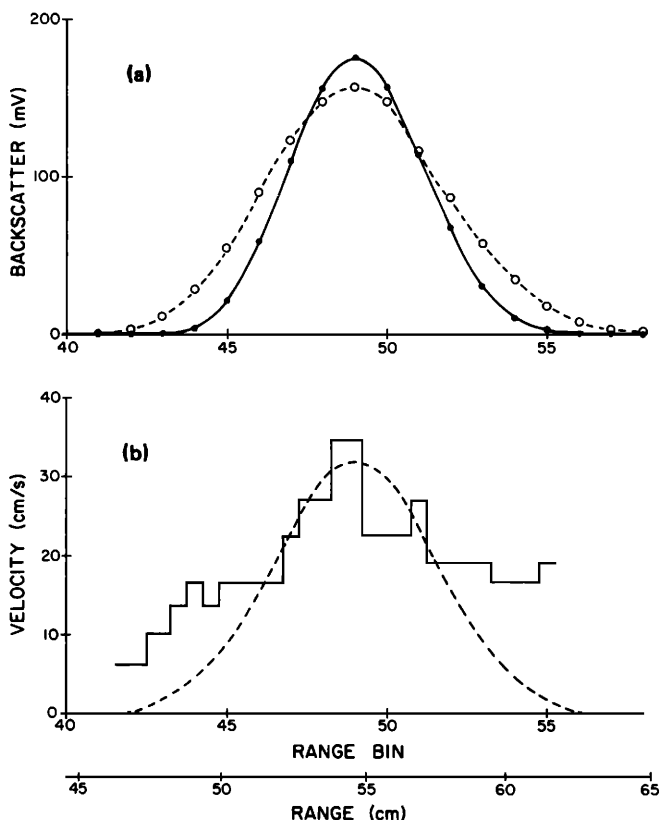


FIG. 19. (a) Time-average backscatter amplitude profiles across the jet as a function of range bin and range, at 2.25 MHz, $h = 28$ cm and at 5.00 MHz, $h = 41.5$ cm. (b) Velocity profile at $h = 35.25$ cm estimated from two-point correlation between 2.25- and 5-MHz backscatter. Dashed line represents $W = 32 \exp[-x^2/2(2.8)^2]$ cm/s.

would also carry larger than average momentum, this too is quite reasonable.

A more detailed examination of the data in Fig. 17 is provided by two selected segments presented in Figs. 20 and 21, each now normalized by the square root of their variance and each representing a further expansion of the time scale. In each case the correlation function is more sharply peaked than in Fig. 18, and in Fig. 21 especially, a one-to-one correspondence between peaks in the two time series at the appropriate lag is evident. It is clear from Fig. 20, however, that such a one-to-one correspondence is not always apparent. As well, the peaks of the correlation functions in Figs. 20 and 21 do not occur at the same lag, being at 1 s in Fig. 20 and 1.3 s in Fig. 21.

Given the large vertical separation (four jet widths) of the two transducers and allowing for the evolution and spawning of eddies along this intervening path and the three-dimensional character of the eddies and their trajectories, these results can be reconciled with the hypothesis that the large-amplitude fluctuations are caused by eddies in the concentration field. That is, the low peak correlations, shifts in peak lag position among record segments, and the presence only intermittently of a clear one-to-one correspondence between peaks in the two records are all explainable in terms of evolution of the eddies during transit between the two sound beams. Furthermore, the finding that the correlation velocities are higher in the wings than the velocities extrapolated from direct measurements is consistent with this model. The present findings lend support therefore to earlier suggestions³³ that similar fluctuations observed in field data are due to high-concentration vortices.

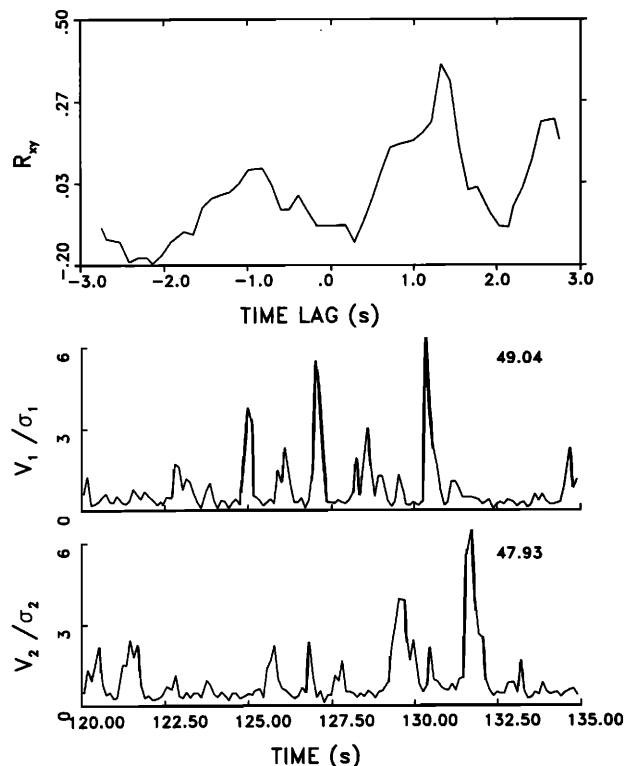


FIG. 21. Backscatter amplitude time series, normalized variance, and cross-correlation function for the 120–135-s segment of Fig. 18.

IV. CONCLUSIONS

It has been shown by using a turbulent circular jet to maintain a quasisteady suspension of solid particles in a localized part of the sound path, that it is possible to obtain measurements of the differential and total scattering cross sections of solid particles. While the accuracy of the differential cross sections (i.e., the backscatter form factor) is usually better than that of the total cross-section measurements, it is argued that in the present set of experiments this is due only to the comparatively lower statistical reliability of the attenuation measurements, there having been a much greater number of pings used to compute the mean backscatter than the mean attenuation.

The cross sections are themselves interesting. Those for lead-glass beads exhibit the expected oblate-prolate resonance at $k_c a = 5$, detected earlier in attenuation measurements.¹⁵ The total cross-section measurements for natural sand, as shown previously,²⁹ exhibit no resonance features and beyond the long-wavelength region are larger than would be expected on the basis of a resonance-free (rigid) spherical scatterer. Here it is now shown that the backscatter cross section for sand also exhibits no sign of resonance or of the diffraction oscillations present even in cross-section spectra for nonresonant (rigid) spherical scatterers. Beyond the long-wavelength region, the measured backscatter cross sections are also greater than would be expected from a spherical scatterer. Each of these effects is attributed to the irregular surfaces of natural sand grains, which inhibit resonance excitation²⁸ and which should lead to larger cross sec-

tions. The backscatter form factor does, however, exhibit the extrema at low $k_c a$, also present in spherical scatterer computations, which are due to the dipole oscillation of the scatterer about its center of mass.¹⁵

It has also been shown that both the attenuation and the squared mean backscatter (at frequencies for which attenuation is negligible) are linear functions of particle concentration up to concentrations of order 25 kg/m^3 or roughly 1% by volume. This represents rather strong empirical confirmation that multiple scattering is unimportant at these concentrations, at least in the size/frequency range spanned by these measurements.

At particle concentrations and frequencies high enough that attenuation due to the particles becomes large, then the observed local backscatter amplitude becomes independent of local particle concentration. This result, which has significant implications for the choice of frequencies used in field investigations of suspended sand transport, is shown to be consistent with theoretical expectations. It was also found in this instance that the measured mean axial attenuation across the jet produces, when applied to the squared mean backscatter, an overcorrection of the results. This apparently cannot be explained solely by the nonuniform geometry of the jet scattering problem, but must also be partly due to the fluctuations in concentration relative to the mean concentration profile across the jet: That is, because the attenuation correction is nonlinear, a time-averaged attenuation measurement applied to a time-averaged backscatter measurement cannot be expected to give the correct result in the presence of large concentration fluctuations.

The concentration fluctuations are indeed large and, at the edge of the jet particularly, produce the same “spikey” behavior in the backscatter amplitude that has been observed in the field.^{1,5,31–34} The question has always been to what degree the peak amplitudes of the spikes in the field data represent actual concentration, since the instrument calibrations are in terms of a fit to time-averaged concentrations. While the measurements here do not prove that the peak concentrations are real in an absolute sense, they do prove that the spikes do indeed carry physically real information on the relative concentration fluctuation field, for the velocity estimates from the two-point correlation measurements are consistent with the measured mean velocity structure of the jet, including even the larger velocities at the edge of the jet that would be expected were the “spikes” in fact eddies carrying higher-than-average concentrations and higher-than-average momentum from the high-concentration, high-momentum core region of the jet.

Finally, it has been necessary as part of the problem of specifying the jet scattering geometry to investigate the behavior of the particle concentration profile as a function of particle size and centerline concentration. The acoustic backscatter results were themselves essential for this purpose and have resulted in an extensive set of measurements of profile width as a function of size and a rather simple relationship between concentration profile width and particle settling velocity.

Thus it is concluded that turbulent circular jets can provide the basis for fundamental investigations of sound scat-

tering by solid particles in turbulent suspensions under quasi-steady conditions and, conversely, that acoustic scattering methods would seem to provide information highly relevant to the dynamics of this type of turbulent two-phase flow.

ACKNOWLEDGMENTS

I thank E. Colbourne and J. Sheng, whose help with the experiments was invaluable and who produced many of the data plots. R. Campbell helped with the computations. L. Huang wrote the original data-acquisition software. R. Guest did the drafting. I am grateful to Dr. A. S. Schaafsma (DELFT HYDRAULICS), who provided the lead-glass beads and useful information on suspended sediment sampling by suction. This work was funded by an Operating Grant from the Natural Sciences and Engineering Research Council of Canada (NSERC), and by an NSERC Strategic Grant (Group) to myself and Dr. A. J. Bowen (Dalhousie University).

APPENDIX: EVALUATING F

The geometric correction factor F in Eq. (13), which accounts for the difference in backscatter intensity from the binwise uniform concentration case (that is, N independent of r , θ , and β within a range interval $r_0 \pm c\tau/4$), has not up to this point been treated explicitly. F is important in two respects. One of these is that the measured mean axial attenuation overcorrects the backscatter at 5 MHz (Fig. 15), and it is apparent that this could be due at least in part to the fact that the mean axial ($\beta = 0$) attenuation must be greater than the mean attenuation at nonzero values of β when the jet concentration profile and acoustic beam are of comparable width. The other reason that F is important relates to the use of system sensitivity constants determined from the jet experiments at low concentration, either those listed in Table III or those based on the calibration curves for a particular sediment type (e.g., Fig. 6), to invert backscatter to suspended sediment concentration in the field.

In the case of a conical jet,

$$N = N_0(z') \exp[-R^2/2\sigma_N^2(z')], \quad (\text{A1})$$

where, from Fig. 5, R is given by

$$R^2 = r^2 \sin^2 \beta \sin^2 \theta + (r \cos \beta - r_0)^2. \quad (\text{A2})$$

Because it is known^{7,16} that the mean concentration of a passive scalar in a turbulent jet obeys equations which are the same as Eqs. (2) and (3) for the mean velocity except for a multiplicative constant and because it has been shown here that the particle concentration profile in the jet is consistent with that expected for a passive scalar (suitably corrected for settling velocity), these equations may be used to obtain expressions for the variation of centerline particle concentration and $\sigma_N(0)$ with z' in the vicinity of $h_0 = 28$ cm. From Eq. (3),

$$\sigma_N(z') = \sigma_N(0)(1 - z'/h_0), \quad (\text{A3})$$

where $h_0 = 28$ cm here, and from Eq. (2),

$$N_0(z') = N_0(0)/(1 - z'/h_0). \quad (\text{A4})$$

Measurements of centerline concentration as function of z' , made as a check on Eq. (A4), are presented in Fig. A1, and it

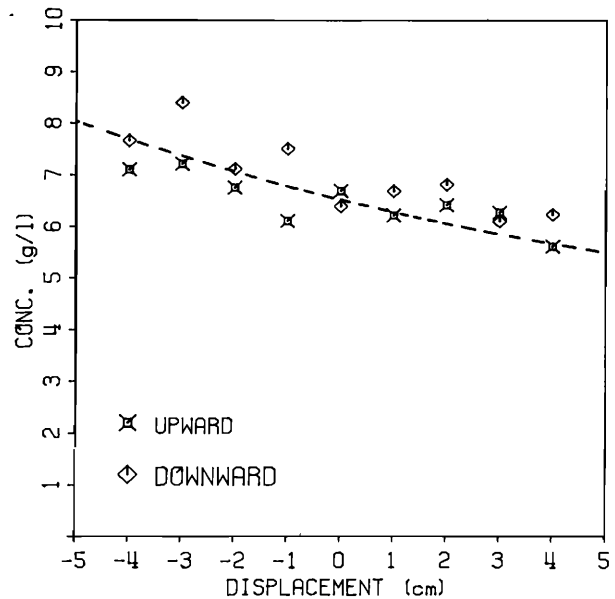


FIG. A1. Centerline concentration measured by suction. Displacements relative to $h_0 = 28$ cm, equal to $-z'$. Symbols represent direction of J -tube displacement: (\diamond) away from nozzle (\square) and toward nozzle. Solid line represents Eq. (A4).

can be seen that the data are acceptably consistent with (A4).

For z' small compared to h_0 , both Eqs. (A3) and (A4) are linear, and since the integration in Eq. (16) is symmetric about $z' = 0$, then the jet may be assumed to be cylindrical when $\beta_m r_0 \ll h_0$. In this case, N and σ_N may be taken to be independent of z' and assume their values at $z' = 0$. The cylindrical jet approximation can be expected to be less accurate when the attenuation coefficient α_p is large, because this will add additional asymmetry about $z' = 0$ beyond that due to the conical jet shape.

1. F at 5 MHz

Values of F , computed using a full three-dimensional numerical integration of Eq. (17) for the long- and short-range 5-MHz measurements in Fig. 14, are presented in Fig. A2. These computations were made on a MIPs 120-5 workstation using a Numerical Algorithms Group (NAG) FORTRAN Library subroutine with $\sigma_N(0) = 1.8$ cm, which, from Fig. 9(d) and Eq. (5), is even smaller than the smallest possible value (1.9 cm) consistent with the measurements [$\sigma_N'(0) \approx 2.05$ cm] and the spatial averaging in the measurement (using $2\sigma = c\tau/2 = 1.5$ cm). Because the importance of the correction factor F increases as the jet concentration profile becomes narrower relative to the transducer beamwidths [inequality (21)], the computed correction factors in Fig. A2 are considered to be the largest possible for the present case: That is, 5-MHz backscatter from Stanhope Beach sand.

The values of F shown in Fig. A2 were computed with the measured 5-MHz directivity pattern [Fig. 4(c)], using cubic spline interpolation between the measured points. Because of the large-amplitude sidelobes for this transducer, computations were made for three values of β_m : 2° , the $-3-$

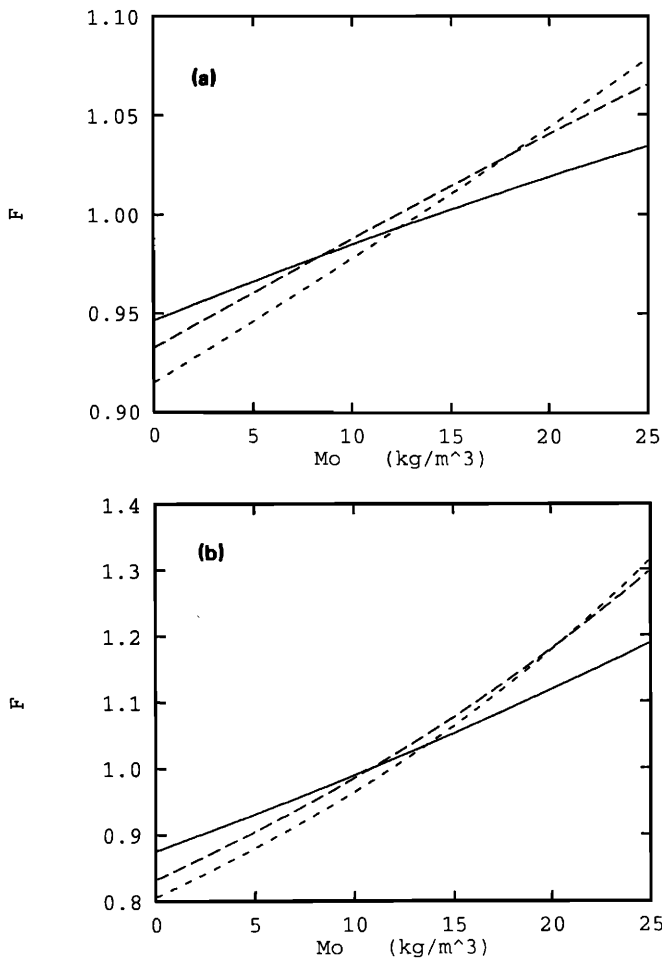


FIG. A2. Geometric correction factor F at 5 MHz from numerical integration of Eq. (17) using cubic spline fit to measured directivity, for $\sigma_N(0) = 1.8$ cm and $\beta_m = 2^\circ$ (solid); 4° (long dashes); and 10° (short dashes). (a) short range, $r_0 = 26.8$ cm; and (b) long range, $r_0 = 53.5$ cm.

dB point; 4° , the full width of the mainlobe; and 10° , the maximum angular extent of the measurements. Consider first the general shapes of these curves. At very low concentrations, $F < 1$, which is expected because particle concentrations decrease away from the jet centerline, and therefore on average the number of particles in the range interval $r_0 \pm c\tau/4$ should be less than in the binwise uniform case. At large concentrations ($M_0 \gtrsim 10$ kg/m³), $F > 1$. This results from the attenuation term, which is unimportant at very low concentration, but which at high concentration is smaller on average than the axial ($\beta = 0$) attenuation A and, because of the exponential dependence, dominates F . At some intermediate concentration, therefore, which in this case occurs at $M_0 \sim 10$ kg/m³, the two effects exactly compensate and $F = 1$.

Note also that the maximum departures of F from unity, at both high and low concentrations, are greater in the long-range case. This too is expected, since in the short-range case the transducer beamwidth is narrower relative to the width of the concentration profile [$\beta(-3 \text{ dB})r_0/2\sigma_N(0) = 0.26$, as opposed to 0.52].

The dependence of F on β_m indicates that, while it can be important to extend the integration beyond the -3 -dB points in the mainlobe, including the large 5-MHz sidelobes affects F only another 2%–3%. This indicates that one need consider only the mainlobe in these experiments, and by implication one may use Eq. (6) and the values of a'_0 in Table II to compute the directivities. In fact, values of F obtained using directivities computed in this way differed by less than 1% maximum from those in Fig. A2 for $\beta_m = 2^\circ$ and 4° .

The values of F at low concentrations (~ 1 kg/m³) do not differ greatly from unity in either case and in the long-range case would result in a maximum error in concentration of 15% and, in $|f_\infty(\pi)|$, of 8%. This is the reason that it was possible to ignore earlier the variations in F with particle size in the determination of system sensitivity constants from the lead-glass bead experiments and the values of $|f_\infty|$ for sand.

Finally, the backscatter results in Fig. 15 were corrected for attenuation using the values of F shown in Fig. A2 for $\beta_m = 10^\circ$.

2. Analytic expression for F

It is possible in the cylindrical jet approximation to obtain Eq. (18), which is an approximate analytic expression for F , valid for $\beta_m r_0/2\sigma_N(0) < 1$. Figure A3 shows comparisons between Eq. (18) and the numerical integration of Eq. (17) for both cylindrical and conical jets, with $\beta_m = 2^\circ$ and $\sigma_N(0) = 1.8$ cm. It can be seen, for cylindrical jets, that the analytic expression is quite accurate at centerline concentrations below 10 kg/m³. It can also be seen that the cylindrical jet approximation is a reasonably good one at both long and short range.

The derivation of Eq. (18) is somewhat complicated and is outlined below. It is convenient to return to Eq. (8), writing down the integral

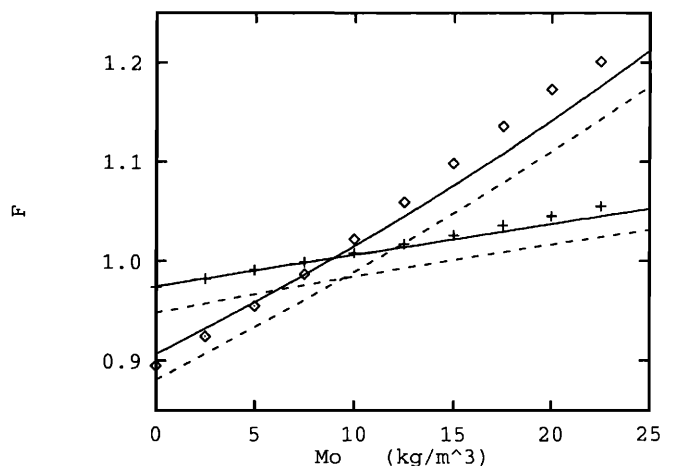


FIG. A3. Comparison between analytic and numerical estimates of F , for $\sigma_N(0) = 1.8$ cm and $\beta_m = 2^\circ$, using directivities computed from Eq. (6). Symbols indicate analytic calculations: (+) short range, $r_0 = 26.8$ cm; and (\diamond) long range, $r_0 = 53.5$ cm. Solid and dashed lines, respectively, indicate numerical integrations for cylindrical and conical jets.

$$I_{r\theta\beta} = \int_{r_0 - c\tau/4}^{r_0 + c\tau/4} \int_0^{2\pi} \int_0^{\beta_m} ND^4 \frac{e^{-4\alpha r}}{r^2} \times \sin \beta d\beta d\theta dr, \quad (A5)$$

and to begin with the radial integration

$$I_r = \int_{r_0 - c\tau/4}^{r_0 + c\tau/4} \frac{Ne^{-4\alpha r}}{r^2} dr. \quad (A6)$$

Then, with $\xi = r - r_0$, R in Eq. (A1) can be written in two useful approximate forms for $\beta^2 \ll 1$:

$$R^2 \approx \xi^2 - \beta^2 r_0 \xi \cos 2\theta + \frac{\beta^2 r_0^2}{2} (1 - \cos 2\theta) \quad (A7)$$

and

$$R^2 \approx \left(\xi - \frac{\beta^2 r_0}{2} \cos 2\theta \right)^2 + \frac{\beta^2 r_0^2}{2} (1 - \cos 2\theta). \quad (A8)$$

Now, using Eq. (A1) for N with $z' = 0$ (the cylindrical jet approximation) and Eq. (9) for α , and noting that, to a good approximation,

$$\int_{-\infty}^l e^{-t^2/2} dt \approx \sqrt{2\pi} (1 + 0.8l)/2, \quad (A9)$$

for $l < 0.4$, then it is possible to show for $c\tau/4 \ll r_0$ that the radial integral is

$$I_r \approx \frac{c\tau}{2} \frac{N(0)}{r_0^2} \Gamma(\beta, \theta) \exp \left[-4\alpha_0 r_0 - A\Gamma(\beta, \theta) \left(1 - 0.4 \frac{\beta^2 r_0}{\sigma_N(0)} \cos 2\theta \right) \right] \times \frac{\sinh \left[\alpha_0 c\tau + 0.4\sqrt{2\pi} B\Gamma(\theta, \beta) - \beta^2 r_0 c\tau \cos 2\theta / 8\sigma_N^2(0) \right]}{\alpha_0 c\tau + 0.4\sqrt{2\pi} B\Gamma(\theta, \beta) - \beta^2 r_0 c\tau \cos 2\theta / 8\sigma_N^2(0)}, \quad (A10)$$

where

$$\Gamma(\beta, \theta) = \exp \left[-b_0^2 (1 - \cos 2\theta) \right], \quad (A11)$$

and $b_0^2 = \beta^2 r_0^2 / 4\sigma_N(0)^2$. At 5 MHz and 20 °C, $\alpha_0 = 0.62 \text{ m}^{-1}$. So, for $\tau = 20 \mu\text{s}$, $\alpha_0 c\tau \sim 2 \times 10^{-2}$, which is much less than unity, as mentioned earlier. Also, for $\beta \sim 2^\circ$ maximum, $r_0 \sim 55 \text{ cm}$, and $\sigma_N(0) = 1.8 \text{ cm}$, $\beta^2 r_0 c\tau / 8\sigma_N^2(0) \sim 0.8 \times 10^{-2}$, and $0.4\beta^2 r_0 / \sigma_N(0) \sim 1.5 \times 10^{-2}$. These terms can therefore be ignored in Eq. (A10), which then becomes

$$I_r \approx \frac{c\tau}{2} \frac{N(0)}{r_0^2} \Gamma \exp(-4\alpha_0 r_0 - A\Gamma) \frac{\sinh B\Gamma}{B\Gamma}, \quad (A12)$$

where use has also been made of the fact that $0.4\sqrt{2\pi} = 1.003 \approx 1.0$. Thus

$$I_{r\theta\beta} = \frac{c\tau}{2} \frac{N(0)}{r_0^2} e^{-4\alpha_0 r_0} \int_0^{2\pi} \int_0^{\beta_m} e^{-A\Gamma} \frac{\sinh B\Gamma}{B} \beta d\beta d\theta, \quad (A13)$$

and the θ integration is then

$$I_\theta = \frac{2}{B} \int_0^{\pi/2} e^{-A\Gamma} (e^{B\Gamma} - e^{-B\Gamma}) d\theta. \quad (A14)$$

This is the interesting part of the problem for, upon substituting for Γ and setting $\phi = 2\theta$, one has an integral of the form

$$I_\phi = e^{-(A \pm B)(1 - b_0^2)} \int_0^{\pi} \exp \left[-(A \pm B) b_0^2 \cos \phi \right] d\phi. \quad (A15)$$

Noting that³⁵

$$e^{iz \cos \phi} = \sum_{n=0}^{\infty} (2n+1) i^n j_n(z) P_n(\cos \phi), \quad (A16)$$

where z is any complex number, $j_n(z)$ is the n th-order spherical Bessel function, and $P_n(\cos \phi)$ the n th-order Legendre polynomial, then with $z = i(A \pm B) b_0^2$, I_ϕ can be written as an infinite series of even- n terms, since the odd- n

Legendre polynomials integrate to zero over the interval $(0, \pi)$. Finally, for $|z| \ll O(1)$, only the $n = 0$ term is important, since $j_0(z)$ tends to unity at the origin, whereas all higher orders tend to zero.³⁶ Therefore,

$$I_\theta \approx \frac{\pi}{B} \left\{ e^{-(A-B)(1-b_0^2)} j_0 [i(A-B)b_0^2] - e^{-(A+B)(1-b_0^2)} j_0 [i(A+B)b_0^2] \right\}. \quad (A17)$$

Finally,

$$I_\theta = -\frac{2\pi e^{-A}}{B(A^2 - B^2)b^2} (A \sinh B + B \cosh B - e^{Ab^2} \{ A \sinh [B(1 - b^2)] + B \cosh [B(1 - b^2)] \}), \quad (A18)$$

where $b = \sqrt{2}b_0$. It is this form which, when expanded in powers of b^2 and substituted in Eq. (A13), gives rise to the analytic expression for F in Eq. (18).

¹R. A. Young, J. T. Merrill, T. L. Clarke, and J. R. Proni, "Acoustic profiling of suspended sediments in the marine bottom boundary layer," *Geophys. Res. Lett.* **9**, 175-178 (1982).

²C. E. Vincent, R. A. Young, and D. J. P. Swift, "On the relationship between bedload and suspended sand transport on the inner shelf, Long Island, N.Y.," *J. Geophys. Res.* **87**, 4163-4170 (1982).

³P. D. Thorne, A. P. Salkield, and A. J. Marks, "Application of acoustic techniques to sediment transport studies," in *Acoustics and the Sea Bed*, edited by N.G. Pace (Bath U.P., Bath, U.K. 1983), pp. 395-402.

⁴F. R. Hess and K. W. Bedford, "Acoustic Backscatter System (ABSS): the instrument and some preliminary results," *Mar. Geol.* **66**, 357-379 (1985); J. F. Lynch, "Theoretical analysis of ABSS data for HEBBLE," *Mar. Geol.* **66**, 277-289 (1985).

⁵A. E. Hay, L. Huang, E. B. Colbourne, J. Sheng, and A. J. Bowen, "A high speed multi-channel data acquisition system for remote acoustic sediment transport studies," in *Oceans '88 Proceedings* (IEEE, Baltimore, 1988), Vol. 2, pp. 413-418.

⁶T. Tamura and D. M. Hanes, "Laboratory calibration of a 3 MegaHertz acoustic concentration meter to measure suspended sand concentration,"

- University of Miami, Rosenstiel School of Marine and Atmospheric Science Tech. Rep. 86-004, 1986.
- ⁷E. J. List, "Turbulent jets and plumes," *Annu. Rev. Fluid. Mech.* **14**, 189–212 (1982).
- ⁸G. M. Faeth, "Mixing, transport and combustion of sprays," *Prog. Energy Combust. Sci.* **13**, 293–345 (1987).
- ⁹W. Baerg and W. H. Schwarz, "Measurements of the scattering of sound from turbulence," *J. Acoust. Soc. Am.* **39**, 1125–1132 (1965).
- ¹⁰A. Brandt, "Acoustic return from density fluctuations in turbulent jets," in *Oceans 1975*, 1975 IEEE International Conference on Engineering in the Ocean Environment, San Diego, CA, September 1975 (unpublished).
- ¹¹M. S. Korman and R. T. Beyer, "The scattering of sound by turbulence in water," *J. Acoust. Soc. Am.* **67**, 1980–1987 (1980).
- ¹²R. N. Parthasarathy and G. M. Faeth, "Structure of particle-laden turbulent water jets in still water," *Int. J. Multiphase Flow* **13**, 699–716 (1987).
- ¹³M. J. Crickmore and R. F. Aked, "Pump samplers for measuring sand transport in tidal waters," Conference on Instrumentation in Oceanography, University College of North Wales, Bangor, IERE Conf. Proc. No. 32, 311–326 (1975).
- ¹⁴A. S. Schaafsma, "Development of silt measuring methods; Study of the feasibility of concentration measurement with ultrasound: Results," Report on Investigation F37/M2032 Part II, Delft Hydraulics, November 1988.
- ¹⁵A. E. Hay and A. S. Schaafsma, "Resonance scattering in suspensions," *J. Acoust. Soc. Am.* **85**, 1124–1138 (1989).
- ¹⁶*Procedures in Sedimentary Petrology*, edited by R. E. Carver (Wiley, New York, 1971), p. 653.
- ¹⁷H. B. Fischer, E. J. List, R. C. Koh, J. Imberger, and N. H. Brooks, *Mixing in Coastal and Inland Waters* (Academic, New York, 1979), p. 483.
- ¹⁸J. S. Turner, "Turbulent entrainment: the development of the entrainment assumption, and its application to geophysical flows," *J. Fluid Mech.* **173**, 431–471 (1986).
- ¹⁹J.-S. Shuen, A. S. P. Solomon, Q. F. Zhang, and G. M. Faeth, "Structure of particle-laden jets: measurements and predictions," *Am. Inst. Astronaut. Astronaut. J.* **23**, 396–404 (1985).
- ²⁰S. Elgobashi, T. Abou-Arab, M. Rizk, and A. Mostafa, "Prediction of the particle-laden jet with a two-equation turbulence model," *Int. J. Multiphase Flow* **10**, 697–710 (1984).
- ²¹G. B. Wallis, *One-Dimensional Two Phase Flow* (McGraw-Hill, New York, 1969), p. 408.
- ²²C. S. Clay and H. Medwin, *Acoustical Oceanography: Principles and Applications* (Wiley, New York, 1977), p. 544.
- ²³J. Zemanek, "The beam behavior within the nearfield of a vibrating piston," *J. Acoust. Soc. Am.* **49**, 181–191 (1971).
- ²⁴W. G. Neubauer, R. H. Vogt, and L. R. Dragonette, "Acoustic reflection from elastic spheres. I. Steady-state signals," *J. Acoust. Soc. Am.* **55**, 1123–1129 (1974).
- ²⁵A. E. Hay, "On the remote acoustic detection of suspended sediment at long wavelengths," *J. Geophys. Res.* **88**, 7525–7542 (1983).
- ²⁶P. M. Morse and K. U. Ingard, *Theoretical Acoustics* (McGraw-Hill, New York, 1968), p. 927.
- ²⁷F. H. Fisher and V. P. Simmons, "Sound absorption in sea water," *J. Acoust. Soc. Am.* **62**, 558–564 (1977).
- ²⁸J. J. Faran, Jr., "Sound scattering by solid cylinders and spheres," *J. Acoust. Soc. Am.* **23**, 405–418 (1971); R. Hickling, "Analysis of echoes from a solid elastic sphere in water," *J. Acoust. Soc. Am.* **34**, 1582–1592 (1962); A. E. Hay and D. G. Mercer, "On the theory of sound scattering and viscous absorption in aqueous suspensions at medium and short wavelengths," *J. Acoust. Soc. Am.* **78**, 1761–1771 (1985).
- ²⁹J. Y. Sheng and A. E. Hay, "An examination of the spherical scatterer approximation in aqueous suspensions of sand," *J. Acoust. Soc. Am.* **83**, 598–610 (1988).
- ³⁰V. K. Varadan, V. N. Bringi, V. V. Varadan, and Y. Ma, "Coherent attenuation of acoustic waves by pair-correlated random distributions of scatters with uniform and Gaussian distributions," *J. Acoust. Soc. Am.* **73**, 1941–1947 (1983); Y. Ma, V. K. Varadan, and V. V. Varadan, "Comments on ultrasonic propagation in suspension," *J. Acoust. Soc. Am.* **87**, 2779–2782 (1990).
- ³¹R. K. Johnson, "Sound scattering from a fluid sphere revisited," *J. Acoust. Soc. Am.* **61**, 375–377 (1977).
- ³²J. P. Downing, R. W. Sternberg, and C. R. B. Lister, "New instrumentation for the investigation of sediment suspension processes in the shallow marine environment," *Mar. Geol.* **42**, 19–34 (1981).
- ³³D. M. Hanes and D. A. Huntley, "Continuous measurements of suspended sand concentration in a wave-dominated nearshore environment," *Continental Shelf Res.* **6**, 585–596 (1986).
- ³⁴D. M. Hanes, C. E. Vincent, D. A. Huntley, and T. L. Clarke, "Acoustic measurements of suspended sand concentration in the C^2S^2 experiment at Stanhope Lane, Prince Edward Island," *Mar. Geol.* **81**, 185–186 (1988).
- ³⁵P. M. Morse and H. Feshbach, *Methods of Theoretical Physics* (McGraw-Hill, New York, 1953), Pt. II, p. 1466.
- ³⁶*Handbook of Mathematical Functions*, edited by M. Abramowitz and I. A. Stegun (Dover, New York, 1965), p. 438.